

Primary cilia are not calcium-responsive mechanosensors

M. Delling^{1*}, A. A. Indzhykulyan^{2*}, X. Liu¹, Y. Li², T. Xie³, D. P. Corey² & D. E. Clapham^{1,2}

Primary cilia are solitary, generally non-motile, hair-like protrusions that extend from the surface of cells between cell divisions. Their antenna-like structure leads naturally to the assumption that they sense the surrounding environment, the most common hypothesis being sensation of mechanical force through calcium-permeable ion channels within the cilium¹. This Ca^{2+} -responsive mechanosensor hypothesis for primary cilia has been invoked to explain a large range of biological responses, from control of left–right axis determination in embryonic development to adult progression of polycystic kidney disease and some cancers^{2,3}. Here we report the complete lack of mechanically induced calcium increases in primary cilia, in tissues upon which this hypothesis has been based. We developed a transgenic mouse, *Arl13b-mCherry-GECO1.2*, expressing a ratiometric genetically encoded calcium indicator in all primary cilia. We then measured responses to flow in primary cilia of cultured kidney epithelial cells, kidney thick ascending tubules, crown cells of the embryonic node, kinocilia of inner ear hair cells, and several cell lines. Cilia-specific Ca^{2+} influxes were not observed in physiological or even highly supraphysiological levels of fluid flow. We conclude that mechanosensation, if it originates in primary cilia, is not via calcium signalling.

To examine ciliary Ca^{2+} signalling *in vivo*, we generated transgenic *Arl13b-mCherry-GECO1.2^{tg}* mice in which fluorescent indicators are confined to the primary cilia (Fig. 1a–c and Extended Data Figs 1 and 2). To accurately measure changes in $[\text{Ca}^{2+}]$ in small moving subcellular structures and to control for motion artefacts and differential bleaching of ratioing dyes, we first examined hair cells in the cochlea's organ of Corti, the most sensitive of known Ca^{2+} -responsive mechanosensors (CaRMS)^{4–6}. The apical surface of each hair cell carries a hair bundle with staggered rows of specialized actin-based microvillar projections called 'stereocilia' (Extended Data Fig. 3). Adjacent to the tallest stereocilia is a single non-motile, microtubule-based true cilium (9 + 2; kinocilium). Fine filamentous 'tip links' connect adjacent stereocilia and transmit force to mechano-electrical transduction channels. Mechano-electrical transduction channels open in microseconds, and Ca^{2+} entry rapidly raises $[\text{Ca}^{2+}]$ in stereocilia (10–20 ms time constant)⁷. Using hair cells from the *Arl13b-mCherry-GECO1.2^{tg}* mouse, we can compare $[\text{Ca}^{2+}]$ changes in two structures (stereocilia and kinocilia) of similar geometry (4–10 μm length and 300–600 nm diameter), and determine whether the kinocilium is also a CaRMS, as suggested⁸.

Arl13b-mCherry-GECO1.2 is expressed in all primary cilia of the inner ear sensory epithelium, including kinocilia of both inner hair cells (IHCs) and outer hair cells (OHCs) of the organ of Corti. Scanning electron microscopy at ages embryonic day (E)18 to postnatal (P)3 confirmed normal development of stereocilia bundles in transgenic animals (Extended Data Fig. 3). Fortuitously, some hair cell stereocilia also contained the Ca^{2+} indicator (Fig. 1d and Extended Data Fig. 1d). To test for CaRMS, we applied laminar flow via a micropipette to IHC

bundles (Supplementary Video 1) or kinocilia and imaged via swept field confocal microscopy (up to 1,000 frames per second) to pinpoint the origin of Ca^{2+} influx with high spatial and temporal resolution. Ratioing of GECO1.2 and mCherry fluorescence ($F_{\text{GECO1.2}}/F_{\text{mCherry}}$) reduced movement-related artefacts (see Methods and Supplementary Information). As expected, deflection of the stereocilia bundle resulted in a rapid and robust increase in $F_{\text{GECO1.2}}$ within the bundle, while F_{mCherry} remained largely unchanged (Fig. 1e–g and Supplementary Video 1). IHC bundle deflection increased the ratio approximately threefold (Fig. 2a), slowly recovering to the resting value within 2.5 s after flow application. The slow dissociation rate of Ca^{2+} from GECO1.2 ($\tau \approx 600$ ms; Extended Data Fig. 4) provides a valuable means of distinguishing true changes in $[\text{Ca}^{2+}]$ from movement-related artefacts. In contrast, kinocilia deflected by pressure steps over a range of developmental stages (E14 to P3) exhibited no detectable increase in $[\text{Ca}^{2+}]_{\text{cilium}}$ (Fig. 2b–f and Supplementary Information). We conclude that kinocilia of mouse hair cells, unlike actin-based stereocilia, are not CaRMS.

Next, we examined kidney epithelia primary cilia, widely believed to be CaRMS^{1,3,9}. Primary inner medullary collecting duct (mIMCD) epithelial cells were isolated from kidneys of P14–P21 *Arl13b-mCherry-GECO1.2^{tg/tg}* mice, which express the kidney collecting duct epithelial cell markers, Aquaporin2 (Aqp2; Fig. 1b), and PC2 (Extended Data Fig. 1). *In vivo*, proximal tubule flow velocities are $\sim 300 \mu\text{m s}^{-1}$ (ref. 10). To quantify these forces, we used a flow chamber to measure cilia bending at defined plasma membrane shear stress values in cultured mIMCD cells isolated from *Arl13b-mCherry-GECO1.2^{tg/tg}* mice (Methods and Extended Data Fig. 5). Flow velocities ranging from 3 to 400 $\mu\text{m s}^{-1}$ (shear stress ≈ 0.002 –1 dyn cm^{-2}) bent cilia (Fig. 3a, b) with half maximal bending at 70 $\mu\text{m s}^{-1}$ ($\sim 0.11 \text{ dyn cm}^{-2}$). A similar cilium-bending profile is observed in modelling the cilium as a uniform cylindrical cantilevered beam^{11,12}.

Primary cilia viewed from above were fully deflected by $\sim 250 \mu\text{m s}^{-1}$ flow velocity (Supplementary Video 2 and Fig. 3). Fluorescence intensities immediately dropped as flow flattened the cilium (Fig. 3c, d). Ratioing $F_{\text{GECO1.2}}/F_{\text{mCherry}}$ reduced this motion artefact (Fig. 3e and Extended Data Fig. 6). Imaging cilia from the side was most effective in reducing position/motion/path length artefacts; in this configuration, all parts of the primary cilium are in the same focal plane and never overlie the cell's variable autofluorescence (Fig. 3c, bottom, Supplementary Video 2 and Fig. 3f). Again, no change in $[\text{Ca}^{2+}]_{\text{cilium}}$ was detected during deflection (Fig. 3g, h; digitonin control, Extended Data Fig. 6). Extending our study to other cell types, we found no CaRMS in osteocyte-like cells, mouse embryonic fibroblasts, or, indeed, any primary cilia examined (Extended Data Fig. 7). Instead, we found that in all cases where $[\text{Ca}^{2+}]_{\text{cilium}}$ increased, the Ca^{2+} rise was initiated at other sites in the cell and diffused from the cytoplasm into the cilium (Extended Data Figs 8 and 9 and Supplementary Video 3). At low image acquisition rates (>200 ms per frame), this could easily be

¹Department of Cardiology, Howard Hughes Medical Institute, Boston Children's Hospital, Boston, Massachusetts 02115, USA. ²Department of Neurobiology, Howard Hughes Medical Institute, Harvard Medical School, Boston, Massachusetts 02115, USA. ³Image and Data Analysis Core (IDAC), Harvard Medical School, Boston, Massachusetts 02115, USA.

*These authors contributed equally to this work.

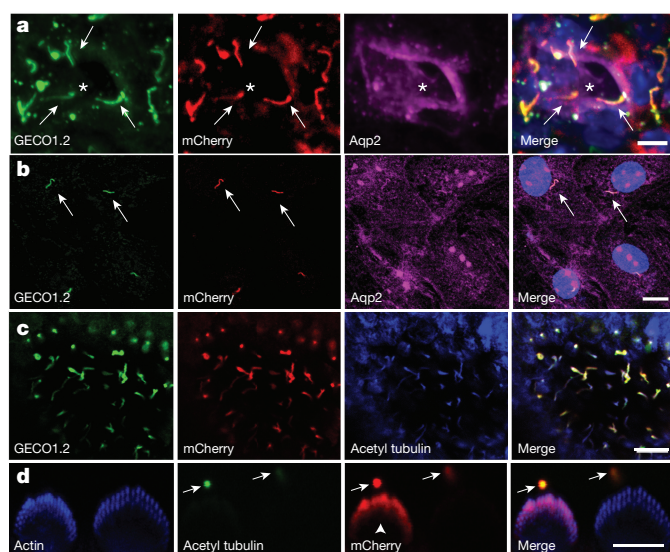
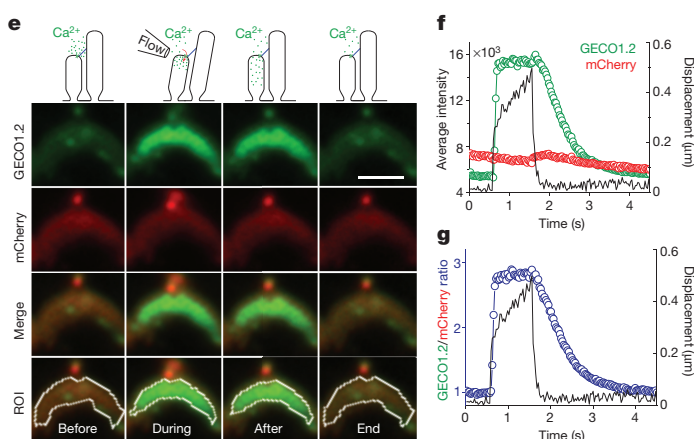


Figure 1 | Genetically encoded Ca^{2+} indicator localizes to primary cilia and cochlear hair cell bundles. **a**, P14 kidney section expressing Arl13b-mCherry-GECO1.2 in primary cilia. Cilia (white arrows) point into the lumen of an aquaporin-2-positive tubule (*). Scale bar, 5 μm . **b**, Aqp2 in primary epithelial cells isolated and cultured (3 days *in vitro*) from kidney papilla of P14–P21 Arl13b-mCherry-GECO1.2^{tg/tg} mice (Extended Data Fig. 1). Scale bar, 10 μm . **c**, Embryonic node from an Arl13b-mCherry-GECO1.2^{tg} mouse. mCherry and GECO1.2 in cilia of the embryonic node overlap with the cilia marker, acetylated tubulin. Scale bar, 10 μm . **d**, Arl13b-mCherry-GECO1.2 expression in IHCs. P4 organ of Corti explant showing two hair bundles; mCherry fluorescence (red), phalloidin-labelled actin (blue), and antibody to acetylated tubulin (green). Arl13b-mCherry-GECO1.2 protein localizes to all kinocilia as demonstrated by overlapping acetylated tubulin staining (arrows). Later in development, Arl13b-mCherry-GECO1.2 also localizes to stereocilia



bundles of some IHCs and OHCs (mCherry-positive bundle, arrowhead; Extended Data Fig. 1). Scale bar, 5 μm . **e–g**, Deflection of IHC stereocilia bundle. Region of interest (ROI): white outline. **e**, $F_{\text{GECO1.2}}$ and F_{mCherry} in stereocilia before, during, and after deflection. A 1 s flow stimulus (Supplementary Video 1) increased $F_{\text{GECO1.2}}$ as Ca^{2+} entered the shorter rows of stereocilia. Scale bar, 5 μm . **f**, Average $F_{\text{GECO1.2}}$ and F_{mCherry} intensities (in arbitrary units) within the ROI; bundle displacement during deflection (black). Deflection increased $F_{\text{GECO1.2}}$ threefold; mCherry bleached only slightly. **g**, Change of stereocilia $F_{\text{GECO1.2}}/F_{\text{mCherry}}$ during the deflection (blue symbols); bundle displacement, black. After stimulus, the bundle rapidly returned to its resting position while Ca^{2+} fluorescence, $F_{\text{GECO1.2}}$, decayed slowly ($\tau = 0.6$ s; Extended Data Fig. 4a, b). Images acquired sequentially, 30 ms per paired frame. All images are representative of more than ten images taken of biological triplicates.

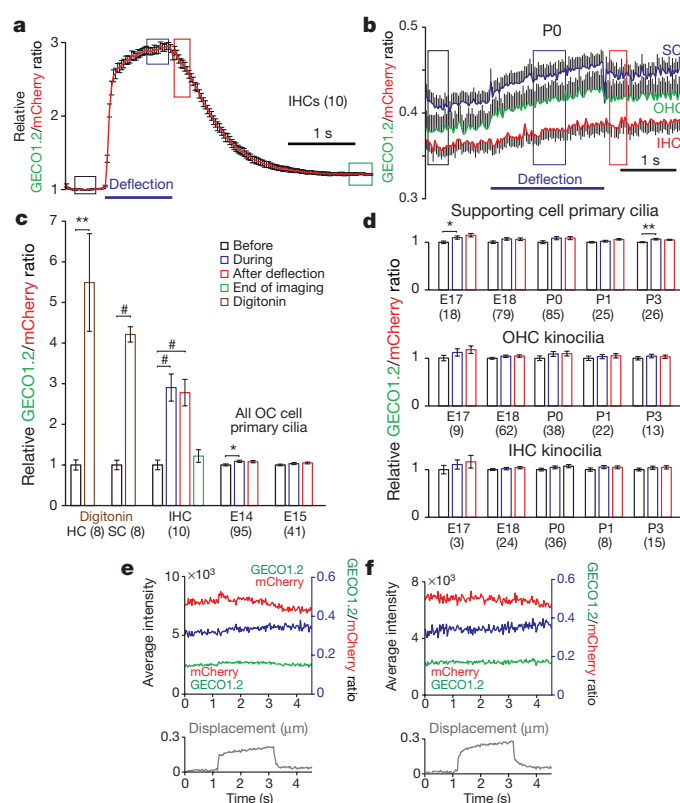


Figure 2 | No change in $[\text{Ca}^{2+}]_{\text{cilium}}$ in kinocilia of developing hair cells. **a**, Average ratio changes in stereocilia for IHC bundle deflections in P5 + 3 days *in vitro* organ of Corti explants (n in brackets). **b**, Average ratio changes for IHC kinocilia (red, $n = 36$), OHC kinocilia (green, $n = 38$), and supporting-cell (SC) primary cilia (blue; $n = 85$). The small positive slope results from differential dye bleaching (mCherry > GECO1.2). **c**, Normalized average fluorescent ratio changes at times boxed in **a** and **b**. Digitonin applied locally to permeabilize the membrane evoked an approximately fivefold ratio increase in hair cell kinocilia and SC primary cilia (brown bars). Black bar, normalized ratio before application; blue bar, during application; red bar, after application. IHC bundle deflection increased stereocilia ratios approximately threefold, persisting well after the bundle returned to its initial position. E14 and E15 explants showed no ratio change in any organ of Corti (OC) primary cilia. **d**, Kinocilia of IHC, OHC, and SC, from E17 to P3, show no ratio change upon deflection. The slight variability of the ratios from the SC cilia (before, during, after) is similar to the variability of the ratios in IHC and OHC kinocilia. **e**, **f**, Individual IHC (**e**) and OHC (**f**) kinocilia at P0. $F_{\text{GECO1.2}}$ (green) and F_{mCherry} (red) intensities (in arbitrary units) and their ratio (blue) show no Ca^{2+} influx upon deflection. Kinocilium displacement in grey (bottom panel). Student's t -test, * $P < 0.05$, ** $P < 0.01$, # $P < 0.001$. All error bars \pm s.e.m.

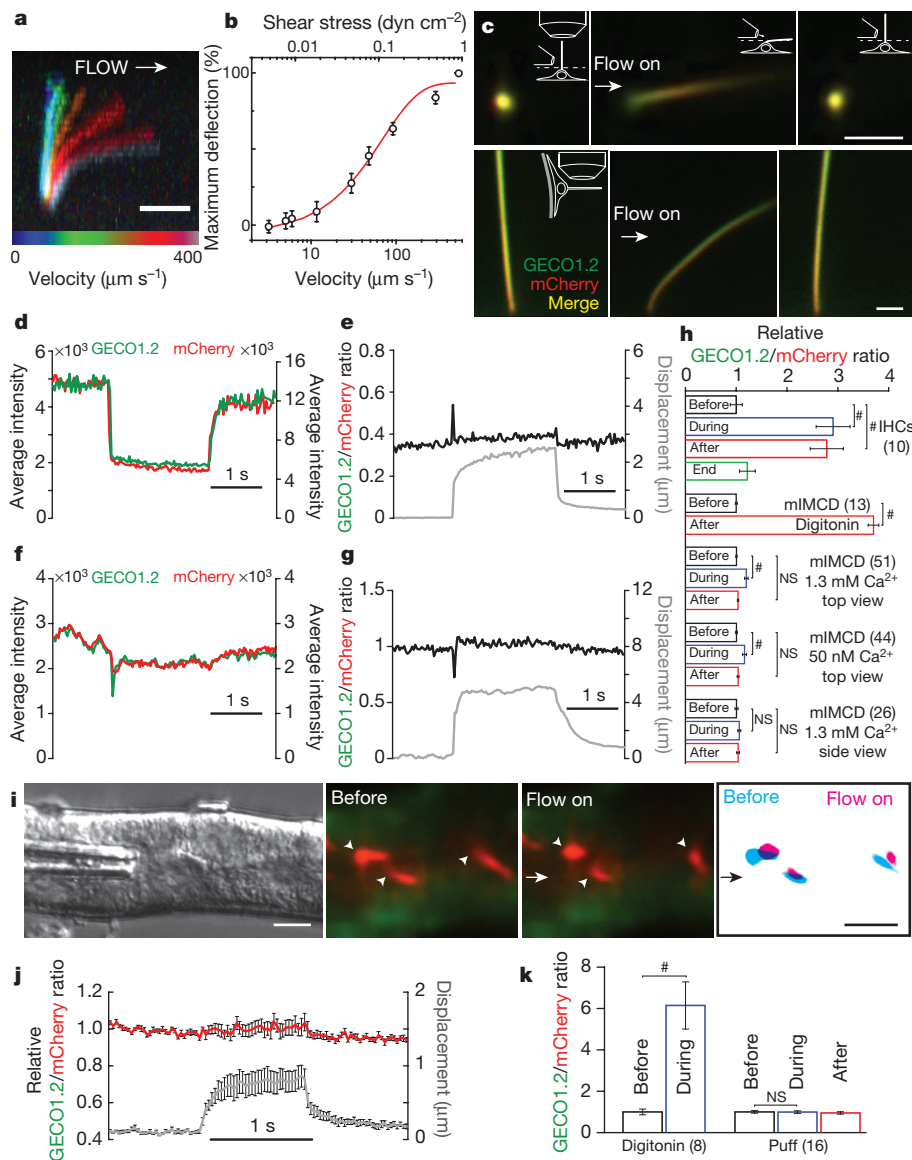


Figure 3 | No change in $[Ca^{2+}]_{cilium}$ during mechanical stimulation of kidney primary cilia. **a**, mIMCD primary cilia at eight flow velocities (Extended Data Fig. 5). Scale bar, 5 μ m; representative of 14 cilia (8 z-stacks, 12 focal planes each). **b**, Cilium deflection as a function of flow velocity and shear stress ($n = 14$). **c**, Cultured primary mIMCD cells from P14–P21 *Arl13b-mCherry-GECO1.2^{tg/tg}* mice imaged from above (top panels, 87 videos, 150 frames each) or the side (bottom, 32 videos \times 150 frames); pipette ~ 4 – 6 μ m from cilium (Supplementary Video 2). Images: before, during, after 2 s, ~ 250 μ m s^{-1} flow velocity stimulus. A MATLAB tracking algorithm identified the ROI frame-by-frame and quantified $F_{GECO1.2}$ and $F_{mCherry}$. Scale bars, 2 μ m; **d**, Channel intensities (in arbitrary units) from top panel in **c**. When flow flattened cilia, average $F_{GECO1.2}$ and $F_{mCherry}$ signals decreased owing to changes in the light path. **e**, Ratioing $F_{GECO1.2}$ to $F_{mCherry}$ reduced artefact (Extended Data Fig. 6), revealing no change in $[Ca^{2+}]$ during deflection. **f**, Side view fluorescence of bottom panel in **c**; $F_{GECO1.2}$ and $F_{mCherry}$ were relatively constant. **g**, Side-viewed $F_{GECO1.2}/F_{mCherry}$ ratio unchanged by deflection. **h**, Normalized $F_{GECO1.2}/F_{mCherry}$ for positive controls (IHC stereocilia bundle deflection; data from Fig. 2c, and digitonin application); and for mIMCD primary cilia deflections in high and low $[Ca^{2+}]$, n in brackets. Small ratio differences are due to motion artefact (Supplementary Information and Extended Data Fig. 6). **i**, Perfusion of acutely dissected kidney thick ascending limb tubules (representative of four preparations) (Extended Data Fig. 5). Green, $F_{GECO1.2}$ and cytoplasmic autofluorescence; red, $F_{mCherry}$. A train of increasing 1 s pressure steps deflected intratubular cilia (arrowheads; Supplementary Video 5). Right, $F_{mCherry}$ overlay from images before (cyan) and during (magenta) cilia deflection. Scale bars, 5 μ m; 16 videos \times 200 frames (middle). **j**, No change in $[Ca^{2+}]_{cilium}$ for the smallest displacement in **i**. **k**, No change in $[Ca^{2+}]_{cilium}$ before, during, and after deflection, data from **j** (1.0 ± 0.06 before versus 0.99 ± 0.06 during, $n = 16$ cilia). Student's t -test, $\#P < 0.001$, NS, not significant. Error bars \pm s.e.m.

misinterpreted as cilia CaRMS^{3,9,13–15}. At very high, non-physiological flow velocities and shear stresses (peak, 10 dyn cm^{-1} (refs 2, 16)), we observed that some cilia tips were ripped from the axoneme (Extended Data Fig. 9 and Supplementary Video 4) and external 2 mM Ca^{2+} filled the breached cilium¹⁷.

In intact kidney tubules, primary cilia are deflected in a pulsatile pattern¹⁸. We microdissected kidney tubules from P21 mice and deflected primary cilia inside isolated tubules (Extended Data Fig. 5). A train of 1 s stepped-amplitude flow stimuli in the lumen facilitated determination of the minimal flow deflecting cilia. Even flow sufficient to fully deflect cilia, however, did not change $[Ca^{2+}]_{cilium}$. Digitonin control increased Ca^{2+} ratios approximately sixfold (Fig. 3i–k and Supplementary Video 5).

During embryonic development, structures that are initially symmetric along the body axis develop a left–right orientation. This orientation depends on cilia in the embryonic node, a depression at the distal tip of the embryo¹⁹. Specialized motile cilia (Supplementary Video 6) in the central node direct fluid leftwards (viewed dorsally) at ~ 2 – 4 $\mu\text{m s}^{-1}$, which is believed to initiate asymmetric gene expression across the node²⁰. Disruption of flow or mutations in primary cilia proteins result in left–right patterning defects²¹ such as situs inversus, while imposed fluid flow to the right side reverts left–right patterning^{22,23}. A prominent hypothesis is that left-side crown cell primary cilia

are deflected by this flow, which mechanically activates ion channels in primary cilia and raises intracellular $[Ca^{2+}]$, leading to altered signalling and gene transcription in those cells and adjacent lateral plate mesoderm^{2,24}. An alternative hypothesis is that the directed beating of nodal cilia creates a gradient of vesicles²⁵ or a secreted morphogen²⁶.

To test the mechanosensitive model, we measured $[Ca^{2+}]$ during deflection of left- and right-side nodal primary cilia (Fig. 4a, b, k, Extended Data Fig. 10 and Supplementary Videos 7 and 8). Cilia from developmental stages ‘early allantoic bud’ to two-somite were mechanically stimulated by applying flow using physiological levels (ramp from 0 $\mu\text{m s}^{-1}$ to ~ 10 $\mu\text{m s}^{-1}$), or supraphysiological flow velocity of ~ 200 $\mu\text{m s}^{-1}$, similar to that previously shown to revert embryonic organ symmetry (Fig. 4b, c)²². Deflection of left- or right-sided nodal cilia did not change $[Ca^{2+}]_{cilium}$ (Fig. 4d–i). These results demonstrate that primary cilia of the embryonic node are not CaRMS from physiological flow velocities to those 50–100 times greater. Notably, physiologically relevant flow velocities (less than ~ 10 $\mu\text{m s}^{-1}$) barely deflected nodal crown cilia (458 ± 22 nm; Fig. 4k–p, Extended Data Fig. 10 and Supplementary Video 9) as predicted (Fig. 3a, b). Resting $[Ca^{2+}]$ was ~ 300 nM both in left- and in right-side cilia (Fig. 4j; for cytoplasmic calcium see ref. 23).

In summary, mechanical forces do not evoke Ca^{2+} signalling within up to 10 s of stimulation in the cilia of kidney tubules, the embryonic

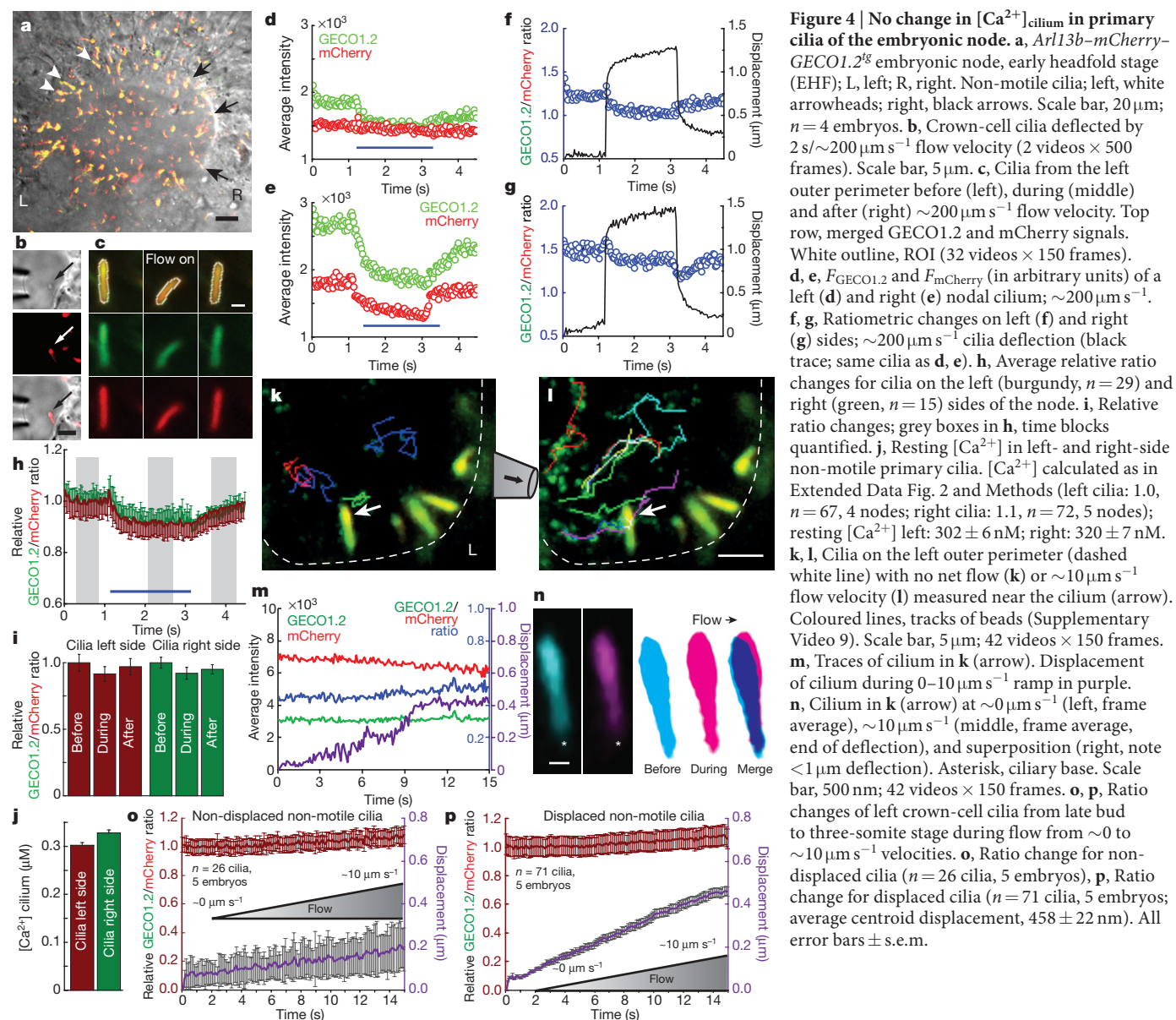


Figure 4 | No change in $[Ca^{2+}]_{\text{cilia}}$ in primary cilia of the embryonic node. **a**, *Arl13b-mCherry-GECO1.2*²⁸ embryonic node, early headfold stage (EHF); L, left; R, right. Non-motile cilia; left, white arrowheads; right, black arrows. Scale bar, 20 μm ; $n = 4$ embryos. **b**, Crown-cell cilia deflected by $2 \text{ s}/\sim 200 \mu\text{m s}^{-1}$ flow velocity (2 videos \times 500 frames). Scale bar, 5 μm . **c**, Cilia from the left outer perimeter before (left), during (middle) and after (right) $\sim 200 \mu\text{m s}^{-1}$ flow velocity. Top row, merged GECO1.2 and mCherry signals. White outline, ROI (32 videos \times 150 frames). **d**, **e**, $F_{\text{GECO1.2}}$ and F_{mCherry} (in arbitrary units) of a left (**d**) and right (**e**) nodal cilium; $\sim 200 \mu\text{m s}^{-1}$. **f**, **g**, Ratiometric changes on left (**f**) and right (**g**) sides; $\sim 200 \mu\text{m s}^{-1}$ cilium deflection (black trace; same cilia as **d**, **e**). **h**, Average relative ratio changes for cilia on the left (burgundy, $n = 29$) and right (green, $n = 15$) sides of the node. **i**, Relative ratio changes; grey boxes in **h**, time blocks quantified. **j**, Resting $[Ca^{2+}]$ in left- and right-side non-motile primary cilia. $[Ca^{2+}]$ calculated as in Extended Data Fig. 2 and Methods (left cilia: 1.0, $n = 67$, 4 nodes; right cilia: 1.1, $n = 72$, 5 nodes); resting $[Ca^{2+}]$ left: $302 \pm 6 \text{ nM}$; right: $320 \pm 7 \text{ nM}$. **k**, **l**, Cilia on the left outer perimeter (dashed white line) with no net flow (**k**) or $\sim 10 \mu\text{m s}^{-1}$ flow velocity (**l**) measured near the cilium (arrow). Coloured lines, tracks of beads (Supplementary Video 9). Scale bar, 5 μm ; 42 videos \times 150 frames. **m**, Traces of cilium in **k** (arrow). Displacement of cilium during 0 – $10 \mu\text{m s}^{-1}$ ramp in purple. **n**, Cilium in **k** (arrow) at $\sim 0 \mu\text{m s}^{-1}$ (left, frame average), $\sim 10 \mu\text{m s}^{-1}$ (middle, frame average, end of deflection), and superposition (right, note $< 1 \mu\text{m}$ deflection). Asterisk, ciliary base. Scale bar, 500 nm; 42 videos \times 150 frames. **o**, **p**, Ratio changes of left crown-cell cilia from late bud to three-somite stage during flow from ~ 0 to $\sim 10 \mu\text{m s}^{-1}$ velocities. **o**, Ratio change for non-displaced cilia ($n = 26$ cilia, 5 embryos), **p**, Ratio change for displaced cilia ($n = 71$ cilia, 5 embryos); average centroid displacement, $458 \pm 22 \text{ nm}$. All error bars \pm s.e.m.

node, several cell lines used as models of cilia function, or kinocilia. Since mechanosensitive channels and putative mechanically gated G-protein-coupled receptors respond in the $10 \mu\text{s}$ to 100 ms range^{27,28}, we suspect the reported increases in $[Ca^{2+}]_{\text{cilia}}$ after ~ 10 – 20 s stimulation^{3,15} originate from the cell body. Indeed, imaging up to 100 Hz revealed that non-ciliary origins were always the initial site of $\Delta[Ca^{2+}]$ (Extended Data Figs 8 and 9 and Supplementary Video 3) and the Ca^{2+} wave initiated in the cytoplasm propagated into the primary cilium. To account for previous observations, we speculate that the two primary sources of error were (1) insufficient time resolution— Ca^{2+} originating from the cytoplasm can diffuse into the cilium in $< 200 \text{ ms}$ and be mistaken as originating from within the cilium, and (2) motion- and light-path-dependent artefacts. Finally, we do not imply that there are no mechanosensitive elements in primary cilia in physiologically relevant ranges, since motor, cytoskeletal, and other proteins are affected by changes in geometry and force without changes in ciliary $[Ca^{2+}]$ ²⁹. An important implication of these findings is that situs inversus and polycystic kidney disease caused by the loss of polycystins^{23,30} are not due to loss of mechanically induced cilia-initiated calcium signalling. These data should motivate investigators to focus on other potential mechanisms for regulation of ciliary ion

channels, and to determine whether calcium propagation into the cilium from the cytoplasm affects ciliary function.

Online Content Methods, along with any additional Extended Data display items and Source Data, are available in the online version of the paper; references unique to these sections appear only in the online paper.

Received 22 May 2015; accepted 16 February 2016.

Published online 23 March 2016.

- Zimmerman, K. & Yoder, B. K. Snapshot: sensing and signaling by cilia. *Cell* **161**, 692–2.e1 (2015).
- Hamada, H. Role of physical forces in embryonic development. *Semin. Cell Dev. Biol.* **47–48**, 88–91 (2015).
- Nauli, S. M. *et al.* Polycystins 1 and 2 mediate mechanosensation in the primary cilium of kidney cells. *Nature Genet.* **33**, 129–137 (2003).
- Corey, D. P. & Hudspeth, A. J. Ionic basis of the receptor potential in a vertebrate hair cell. *Nature* **281**, 675–677 (1979).
- Corey, D. P. & Hudspeth, A. J. Response latency of vertebrate hair cells. *Biophys. J.* **26**, 499–506 (1979).
- Sellick, P. M., Patuzzi, R. & Johnstone, B. M. Measurement of basilar membrane motion in the guinea pig using the Mössbauer technique. *J. Acoust. Soc. Am.* **72**, 131–141 (1982).
- Beurg, M., Fettiplace, R., Nam, J. H. & Ricci, A. J. Localization of inner hair cell mechanotransducer channels using high-speed calcium imaging. *Nature Neurosci.* **12**, 553–558 (2009).

8. Kindt, K. S., Finch, G. & Nicolson, T. Kinocilia mediate mechanosensitivity in developing zebrafish hair cells. *Dev. Cell* **23**, 329–341 (2012).
9. Praetorius, H. A. & Spring, K. R. Bending the MDCK cell primary cilium increases intracellular calcium. *J. Membr. Biol.* **184**, 71–79 (2001).
10. Weinstein, A. M. A mathematical model of rat ascending Henle limb. III. Tubular function. *Am. J. Physiol. Renal Physiol.* **298**, F543–F556 (2010).
11. Schwartz, E. A., Leonard, M. L., Bizios, R. & Bowser, S. S. Analysis and modeling of the primary cilium bending response to fluid shear. *Am. J. Physiol.* **272**, F132–F138 (1997).
12. Young, Y. N., Downs, M. & Jacobs, C. R. Dynamics of the primary cilium in shear flow. *Biophys. J.* **103**, 629–639 (2012).
13. AbouAlaiwi, W. A. *et al.* Ciliary polycystin-2 is a mechanosensitive calcium channel involved in nitric oxide signaling cascades. *Circ. Res.* **104**, 860–869 (2009).
14. Jin, X. *et al.* Cilioplasm is a cellular compartment for calcium signaling in response to mechanical and chemical stimuli. *Cell. Mol. Life Sci.* **71**, 2165–2178 (2014).
15. Su, S. *et al.* Genetically encoded calcium indicator illuminates calcium dynamics in primary cilia. *Nature Methods* **10**, 1105–1107 (2013).
16. Lee, K. L. *et al.* The primary cilium functions as a mechanical and calcium signaling nexus. *Cilia* **4**, 7 (2015).
17. Delling, M., DeCaen, P. G., Doerner, J. F., Febvay, S. & Clapham, D. E. Primary cilia are specialized calcium signalling organelles. *Nature* **504**, 311–314 (2013).
18. O'Connor, A. K. *et al.* An inducible CiliaGFP mouse model for *in vivo* visualization and analysis of cilia in live tissue. *Cilia* **2**, 8 (2013).
19. Lee, J. D. & Anderson, K. V. Morphogenesis of the node and notochord: the cellular basis for the establishment and maintenance of left-right asymmetry in the mouse. *Dev. Dyn.* **237**, 3464–3476 (2008).
20. Okada, Y., Takeda, S., Tanaka, Y., Izpisua Belmonte, J. C. & Hirokawa, N. Mechanism of nodal flow: a conserved symmetry breaking event in left-right axis determination. *Cell* **121**, 633–644 (2005).
21. Nonaka, S. *et al.* Randomization of left-right asymmetry due to loss of nodal cilia generating leftward flow of extraembryonic fluid in mice lacking KIF3B motor protein. *Cell* **95**, 829–837 (1998).
22. Nonaka, S., Shiratori, H., Saijoh, Y. & Hamada, H. Determination of left-right patterning of the mouse embryo by artificial nodal flow. *Nature* **418**, 96–99 (2002).
23. Yoshida, S. *et al.* Cilia at the node of mouse embryos sense fluid flow for left-right determination via Pkd2. *Science* **338**, 226–231 (2012).
24. McGrath, J., Somlo, S., Makova, S., Tian, X. & Brueckner, M. Two populations of node monocilia initiate left-right asymmetry in the mouse. *Cell* **114**, 61–73 (2003).
25. Tanaka, Y., Okada, Y. & Hirokawa, N. FGF-induced vesicular release of Sonic hedgehog and retinoic acid in leftward nodal flow is critical for left-right determination. *Nature* **435**, 172–177 (2005).
26. Okada, Y. *et al.* Abnormal nodal flow precedes situs inversus in *iv* and *inv* mice. *Mol. Cell* **4**, 459–468 (1999).
27. Xiao, R. & Xu, X. Z. Mechanosensitive channels: in touch with Piezo. *Curr. Biol.* **20**, R936–R938 (2010).
28. Connelly, T. *et al.* G protein-coupled odorant receptors underlie mechanosensitivity in mammalian olfactory sensory neurons. *Proc. Natl Acad. Sci. USA* **112**, 590–595 (2015).
29. Iskratsch, T., Wolfenson, H. & Sheetz, M. P. Appreciating force and shape — the rise of mechanotransduction in cell biology. *Nature Rev. Mol. Cell Biol.* **15**, 825–833 (2014).
30. Ma, M., Tian, X., Igarashi, P., Pazour, G. J. & Somlo, S. Loss of cilia suppresses cyst growth in genetic models of autosomal dominant polycystic kidney disease. *Nature Genet.* **45**, 1004–1012 (2013).

Supplementary Information is available in the online version of the paper.

Acknowledgements We thank the Mouse Gene Manipulation Facility of the Boston Children's Hospital Intellectual and Developmental Disabilities Research Center (IDDR; NIH30-HD 18655), National Institutes of Health (NIH) 5R01 DC000304 to D.P.C., and the Kaplan Family for financial support to M.D. We thank J. Rivera, J. Angelo, J. Mager and K. Tremblay for help with developmental staging of mouse embryos, L. Palmer and G. Frindt for teaching M.D. the kidney tubule dissection, A. Weinstein for discussions of fluid velocities in kidney tubules, W. Fowle for access to the scanning electron microscopy facility, R. Stepanyan and J. Shen for help with statistics, and members of the Clapham and Corey laboratories for advice and discussion. We thank H. Zeng for the Ai95 mouse line, L. Bonewald for the MLO-Y4-cell line, P. Divieti Pajevic and J. Spatz for the Ocy454 cell line, and T. Indzhukulian for support. D.E.C. and D.P.C. are Investigators of the Howard Hughes Medical Institute.

Author Contributions M.D. and A.A.I. performed the experiments. X.L. and Y.L. helped with experiments; T.X. developed software for analysis. M.D., A.A.I., D.P.C., and D.E.C. analysed the data and wrote the manuscript.

Author Information Reprints and permissions information is available at www.nature.com/reprints. The authors declare no competing financial interests. Readers are welcome to comment on the online version of the paper. Correspondence and requests for materials should be addressed to D.E.C. (dclapham@enders.tch.harvard.edu) or D.P.C. (dcory@hms.harvard.edu).

METHODS

The experiments were not randomized. The investigators were not blinded to allocation during experiments and outcome assessment.

Molecular biology, transgenic animals. The *Scal*/HindIII linearized *hArl13b-mCherry-GECO1.2* pCAG vector (chicken actin promoter) was gel-purified and injected into the pronucleus of *C57BL6/6J* oocytes at the transgenic animal core facility at Boston Children's Hospital (Boston, Massachusetts). The integration site for the *Arl13b-mCherry-GECO1.2* transgene was determined by genomic walking (Bio S&T). The genotype of transgenic animals was determined by PCR: primers 372-up, ACATGGCCTTTCCTGCTCTC; 372-down, TTCAACATTTCCGTGTCGCC; and 944-down, GACATCTGTGGGAGG AGTGG. PCR product for the wild-type genomic sequence: ~600 bp; transgene PCR product ~400 bp. All animal procedures of this study were approved by the IACUCs of Boston Children's Hospital and Harvard Medical School (Boston, MA). Animals were maintained according to ARCH standards at Boston Children's Hospital and euthanized using CO₂.

Isolation of mIMCD. *Arl13b-mCherry-GECO1.2^{tg}*: mIMCD cells were isolated as described³¹. Briefly, ten kidneys isolated from P14–P21 *Arl13b-mCherry-GECO1.2^{tg}* mice were cut longitudinally with fine scissors and the outer and inner medulla removed. The tissue was cut into small pieces with a razor blade and digested in collagenase (2 mg ml⁻¹) and hyaluronidase (1 mg ml⁻¹) for 1 h at 37°C in L-15 medium (Life Technologies). After trituration of the homogenate, cells were washed twice in phosphate-buffered saline (PBS) and plated on laminin-coated dishes (Life Technologies). Cells were grown in DMEM (adjusted to 600 mOsm with urea and NaCl), containing 200 μM dibutyl-*c*-AMP (db-*c*-AMP), unless stated otherwise. After 2 days, cells were split on laminin-coated coverslips (NeuVito) and imaged after culturing for an additional 1–2 days to allow confluent cell growth. For side-view imaging, cells were grown on 24 mm Transwell inserts (Corning) until they reached confluency. The membrane was excised with a scalpel and folded before imaging. Where indicated, mIMCD cells were serum starved in DMEM containing 0.2% BSA for 24 h or 48 h. Imaging solutions: L-15 medium (1.3 mM Ca²⁺) or HEPES-containing solution buffered to 50 nM [Ca²⁺] (see 'Calibration of the ratiometric *Arl13b-mCherry-GECO1.2* sensor' for buffer composition).

Microdissection of *Arl13b-mCherry-GECO1.2^{tg}* kidney tubules. Microdissection was performed as described previously³² with modifications. In brief, 1-mm thick transverse slices of P14–P21 kidneys were incubated with collagenase (1 mg ml⁻¹) and hyaluronidase (1 mg ml⁻¹) for 30 min at 37°C in L-15 medium (Life Technologies), or gently dissected without prior treatment. The cortex was removed with fine forceps and bundles of tubules were isolated at the transition of inner (white) and outer (red) medulla (Extended Data Fig. 5c). Thick-walled individual tubules with luminal fluorescent cilia were microdissected and mounted on glass or plastic coverslips coated with Cell-Tak (Corning). Under ×4 magnification (upright Nikon NiE), a micromanipulator-mounted 20° micro-knife (Minitool) was used to cut individual tubules from the bundles. A second micromanipulator held a long-tapered micropipette (bent ~20° to ensure the tip of the pipette was parallel to the surface of the coverslip, Extended Data Fig. 5). Under higher magnification (×100/1.1 numerical aperture or ×60/1.0 numerical aperture water dipping lenses), the micropipette was gently inserted into the tubule lumen and the pressure stimulus applied. Regions of the tubule with no direct micropipette contact were used for Ca²⁺ imaging. In some experiments a third micromanipulator was used to deliver digitonin (20 μM) to the tubules (direct injection into the tubule lumen or external application). Cilia from kidney tubule perfusion experiments were collected from three independent microdissections.

Isolation of *Arl13b-mCherry-GECO1.2^{tg}* and *Arl13b-mCherry-GECO1.2^{tg};GCaMP6f^{tg};E2aCre^{tg}* embryos. *GCaMP6f* (B6;129S-Gt(Rosa)26Sor^{tm95.1(CAG-GCaMP6f)Hze/J}) and *E2a-Cre* (Tg(EIIa-cre)C5379Lmgd) transgenic animals were obtained from Jackson Laboratories. Embryo isolation was performed as described previously³³. Timed pregnancies resulting from mating wild-type *C57BL6/6J*, *Arl13b-mCherry-GECO1.2^{tg}* or *Arl13b-mCherry-GECO1.2^{tg}/1g* females with *Arl13b-mCherry-GECO1.2^{tg}/1g* or *GCaMP6f^{tg}/1g*; *E2a-Cre^{tg}/1g* males yielded embryos that were then selected for the appropriate developmental stages³⁴. Embryos expressing motile cilia in the embryonic node at stages critical for asymmetric gene expression³⁵ (starting at developmental stages 'early allantoic bud' up to two-somite stage) were used for experiments. Embryos were mounted with the embryonic node facing up in a custom-designed embryo mounting plate (Extended Data Fig. 10b–d). Laser cut holes (diameters 0.5–1.2 mm) in 0.8 mm Delrin ensured a good fit of the embryo into the holding well (Extended Fig. 10b, c). All embryonic node imaging was performed in DMEM/F12 with 10% fetal calf serum (Invitrogen).

A similar mating strategy was used to obtain *Arl13b-mCherry-GECO1.2^{tg};GCaMP6f^{tg};E2a-Cre^{tg}* E14 embryos. Mouse embryonic fibroblasts were

isolated from E14 embryos as described previously¹⁷. Where indicated, MEF cells were serum starved in DMEM containing 0.2% BSA for up to 48 h. To visualize cytoplasmic Ca²⁺ oscillations, *Arl13b-mCherry-GECO1.2^{tg};GCaMP6f^{tg};E2a-Cre^{tg}* embryos from late allantoic bud to late headfold stage were used. In brief, embryos were mounted in the upright position as described above and imaged for 4–6 min at a frame rate of 0.5 Hz on an upright FV1000 confocal system (Olympus, ×60/1.1 numerical aperture water dipping lens) at either 36°C or 22°C (room temperature). Cytoplasmic Ca²⁺ oscillations were quantified using ImageJ as described previously³³ with slight modifications: in brief, fluorescence of all frames was averaged and individual frames were divided by average intensity to generate $\Delta F/F$. Images were thresholded to exclude cells with $\Delta F/F$ less than 30%. Furthermore, only regions with area greater than 90 square pixels and circularities greater than 0.6 were used to define cells with cytoplasmic Ca²⁺ oscillations. All Ca²⁺ oscillations within 50 μm surrounding the embryonic node were analysed for occurrence on the left versus the right side of the node.

Reagents. The following reagents were used: mouse anti-acetylated tubulin (Sigma-Aldrich; T7451); CF 405M phalloidin to stain filamentous actin (Biotium; 00034); goat anti-PC2 (Santa Cruz; G-20 sc-10376), rat anti-mCherry (Life Technologies; M11240), chicken anti-EGFP (Aves Labs; GFP-1020).

Immunocytochemistry, confocal microscopy. Cells or embryos were fixed with 4% paraformaldehyde, permeabilized with 0.2% Triton X-100, and blocked by 10% donkey serum in PBS. Cells were labelled with the indicated antibody followed by secondary donkey anti-rabbit, anti-goat, or anti-mouse fluorescently labelled immunoglobulin-G (IgG) (Life Technologies) and Hoechst 33342 (Life Technologies). Confocal images were obtained using an inverted Olympus FV1000 (×60 1.2 numerical aperture water immersion objective lens) and images processed using ImageJ (NIH).

Immunohistochemistry. Fixed (4% paraformaldehyde) 15 μm frozen tissue sections were permeabilized with 0.5% TX100/PBS (pH 7.4) for 15 min and blocked with PBS containing 5% goat serum, 1% BSA, 0.1% fish gelatin, 0.1% TX-100, and 0.05% Tween20. For primary antibodies raised in mice, endogenous mouse IgGs were blocked by incubating sections with the unconjugated Fab fragment goat anti-mouse IgG for 1 h at room temperature. For goat primary antibodies, donkey serum and donkey secondary antibodies were used. Sections were washed twice in PBS-T, and incubated with primary antibodies in blocking solution overnight at 4°C. Slides were washed twice in PBS-T and goat anti-rabbit/anti-mouse fluorescently-labelled secondary antibodies applied at room temperature for 1 h with Hoechst 33342 (nuclear) dye. Sections were washed twice in PBS-T, mounted in Prolong Gold Antifade (Life Technologies), and imaged (inverted Olympus FV1000; ×60, 1.2 numerical aperture water immersion objective). Images were further processed with ImageJ (NIH).

Ca²⁺-imaging in stereocilia and primary cilia. *Arl13b-mCherry-GECO1.2*-expressing cilia were observed under an upright Nikon NiE microscope (×100, 1.1 numerical aperture, 2.5 working distance) equipped with an Opterra swept-field confocal imaging system (Bruker Nano Technologies) and a Photometrics Evolve 128 liquid-cooled EMCCD camera (128 pixels × 128 pixels, 120 nm effective pixel size). This system enables fast imaging of up to 500–1,000 frames per second (f.p.s.) in low-light conditions. In most cases, tissue was illuminated sequentially by 488 nm (GECO1.2) and 561 nm (mCherry) laser light, and imaged using the full CCD chip (15 ms exposure per channel; 33 f.p.s.). To increase light delivery to the camera and avoid excessive photobleaching, swept-field confocal imaging was performed in slit mode (35 μm).

Measurements of cilia bending and flow velocities. mIMCD and MEF cells isolated from *Arl13b-mCherry-GECO1.2^{tg}* mice were seeded in an IBIDI μ-Slide VI 0.4 flow chamber coated with laminin (see IBIDI Application Note 11; for this chamber, apical membrane shear stress is $\tau = \eta \times 131.6 \times \Phi$, where η is dynamic viscosity (0.01 dyn s⁻¹ cm⁻²) and Φ is flow rate in millilitres per minute. A syringe pump (Harvard Apparatus) delivered steady flow via 10 ml syringes containing L-15 medium. Z-stacks of primary cilia were recorded on an inverted Olympus FV1000 (×60, 1.2 numerical aperture water immersion objective). The bend angle was measured between ciliary base and tip¹⁸. Fluid velocities were measured by imaging the flow of the solution supplemented with 300 nm green fluorescent beads (Sicstar greenF, Micromod) at the focal plane corresponding to ciliary tips at rest. Images were acquired as line scans (2 ms per line) or in continuous scanning mode (64 or 128 ms per frame) and particles tracked using an ImageJ plugin.

Calibration of the ratiometric *Arl13b-mCherry-GECO1.2* sensor. Calibration was performed using an inverted Olympus FV1000 (×60, 1.2 numerical aperture water immersion objective) as described previously¹⁷. In brief, standard solutions of [Ca²⁺] (ranging from 50 nM to 50 μM) were prepared by adjusting the ratio of EGTA and CaCl₂ (MaxChelator) in 137 mM NaCl, 5.4 mM KCl, 10 mM HEPES. After isolation, mIMCD cells were plated onto 12 mm laminin-coated

glass coverslips (Neuvitro) and cultured for 3–4 days to allow cilia formation. For controls, digitonin membrane permeabilization (3 min) was followed by image acquisition in multiple fields of view. Ratios were obtained by dividing the average $F_{\text{GECO1.2}}$ (per ROI, corresponding to a single cilium) by the average F_{mCherry} . The average ratios were plotted as a function of free $[\text{Ca}^{2+}]$ fitted to a sigmoid curve: $y = A_2 + (A_1 - A_2) / (1 + \exp[(x - x_0)/dx])$, where $A_1 = 0.15 \pm 0.03$, $A_2 = 1.58 \pm 0.06$, $x_0 = 442 \pm 25$, $dx = 114 \pm 20$, with $x_0 = K_d$ (the dissociation constant). The K_d of bacterially expressed/purified GECO1.2 was $1.1 \mu\text{M}$ (ref. 36), about twice the K_d measured for our GECO1.2 fusion construct in mammalian cells *in situ*. $[\text{Ca}^{2+}]$ in embryonic node primary cilia was estimated from an R_{min} - and R_{max} -adjusted calibration curve, where both values were calculated from images collected on swept-field confocal imaging system. Late bud to late headfold embryos were permeabilized with $20 \mu\text{M}$ digitonin (5 min) in either 50 nM or $5 \mu\text{M}$ $[\text{Ca}^{2+}]$. Resting values for nodal primary cilia were measured in DMEM/F12 + 10% FCS using the same imaging settings used to calculate R_{min} and R_{max} . Ratios were converted to $[\text{Ca}^{2+}]$ using the adjusted Ca^{2+} calibration curve.

Primary cilia and stereocilia deflections. Primary cilia and stereocilia bundle deflections were performed using a custom-made fluid-jet system. Briefly, the micropipette pressure at the back of the pipette could be rapidly changed to a desired value by supplying vacuum and/or pressurized air via feedback-controlled solenoid valves (5–10 ms rise time for the pressure step stimulus). The micropipette was filled with bath solution and the pressure at the mouth of the pipette carefully adjusted before approaching to the cilium, ensuring that there was no flow applied to the cilium before the onset of the stimulus. Depending on the experimental design, digitonin was applied to the cells either using the fluid-jet pipette, or via an additional pipette positioned near the cilium and connected to an IM-9C microinjector (Narishige).

For kinocilium deflection experiments, organ of Corti explants were acutely dissected and mounted on a coverslip coated with CellTak, or immobilized with tungsten minuten pins (FST). All hair cell imaging experiments were performed at room temperature in L-15 cell culture medium (Invitrogen), containing in mM: NaCl (138), KCl (5.3), CaCl_2 (1.3), MgCl_2 (1.0), Na_2HPO_4 (1.0), KH_2PO_4 (0.44), MgSO_4 (0.81). For stereocilia bundle Ca^{2+} imaging experiments, organ of Corti explants were dissected at P5 in L-15 medium and placed in culture in DMEM/F12 supplemented with 5% FBS and 10 mg l^{-1} ampicillin at 37°C (10% CO_2). Explants were cultured for 3 days to increase the number of cells with sufficient sensor in stereocilia bundles.

All images were analyzed using a custom-made MATLAB tracking algorithm (described below), ImageJ (NIH), and Origin 8 (OriginLab).

Osteocyte-like cell lines MLO-Y4 and Ocy454 (ref. 37) were tested for authenticity in the laboratories that supplied them (see Acknowledgements) and for mycoplasma contamination by our laboratory. Both cell types were transfected with a plasmid encoding *Arl13b-mCherry-GECO1.2* using electroporation (LONZA, solution V, program T-20), as described previously³⁸. Cells were seeded on coverslips after transfection and cultured at 37°C . Cells were used after a primary cilium was visible.

Embryonic node cilia were deflected with either a fast fluid-jet stimulus (described above) or with a ramp of slow, physiological level flow, delivering up to $\sim 10 \mu\text{m s}^{-1}$ velocities: fluid flowed from a gravity-fed open-ended syringe to the micropipette. Flow rates were calibrated using 100 nm fluorescent beads (Sicstar-greenF, Micromod) and adjusted by gently lifting the syringe up 5–10 mm using a coarse micromanipulator. Perfusion fluid contained 100 nm fluorescent beads at $10 \mu\text{g ml}^{-1}$ and was applied directly to the node via micropipette (pipette opening 4–6 μm in diameter) that was 4–6 μm away from the imaging area. Flow rates were adjusted manually as described above such that there was no net flow at the beginning of the experiment and ~ 10 – $12 \mu\text{m s}^{-1}$ velocity at the end of the 15 s imaging experiment. Bead velocities and tracks were quantified and visualized using the 'manual tracking' plugin in ImageJ.

Pipette flow calibration. Pipette flow was calibrated using 300 nm fluorescent beads (Sicstar-greenF, Micromod) re-suspended at 0.5 mg ml^{-1} in DMEM/F12 10% FCS and loaded into micropipettes following sonication. A pressure stimulus was applied to the back of the pipette and steady flow imaged at 1,000 f.p.s. to ensure accurate frame-by-frame reading for each bead position while exiting the pipette and during its travel across the imaging area ($\sim 15 \mu\text{m}$). The 1-ms time resolution of the calibration experiment was sufficient to resolve and calibrate the range of velocities used.

Scanning electron microscopy. Cultured mIMCD cells were fixed for 1 h at room temperature with 2.5% glutaraldehyde (Electron Microscopy Sciences) in 0.1 M sodium cacodylate buffer (pH 7.4), supplemented with 2 mM CaCl_2 , and stored in distilled water. Organ of Corti explants were fixed following Ca^{2+} imaging experiments, or the entire cochlea was fixed, microdissected in distilled water and prepared for scanning electron microscopy as previously described³⁹. Briefly, specimens

were dehydrated in ethanol, critical point dried from liquid CO_2 , mounted on a carbon tape, sputter-coated with 5 nm platinum, and imaged on a Hitachi S-4800 field emission scanning electron microscope.

Data analysis. All images were analysed using a custom-made MATLAB tracking algorithm (described below), ImageJ (NIH), and Origin 8 (OriginLab).

Sample size predetermination (power analysis). In stereocilia we observed a 2.9 ± 1.05 (mean \pm s.d.)-fold change (effect size $d = 2.76$) in $F_{\text{GECO1.2}}/F_{\text{mCherry}}$ after activation of a Ca^{2+} -conducting mechanosensor. Assuming a one-sided, paired *t*-test conducted at the 0.05 level of significance, a minimum of 12 cells would be required to detect an effect size of $d = 1$ in mechanosensitive $[\text{Ca}^{2+}]$ increase post-stimulation with 95% power.

Image analysis. Customized image analyses were developed using MATLAB to automatically process the large volume of ratiometric time-lapse data to improve quantitation and objectivity. The analysis was divided into three steps: channel alignment, object detection, and object tracking over time, with subsequent ratio calculations.

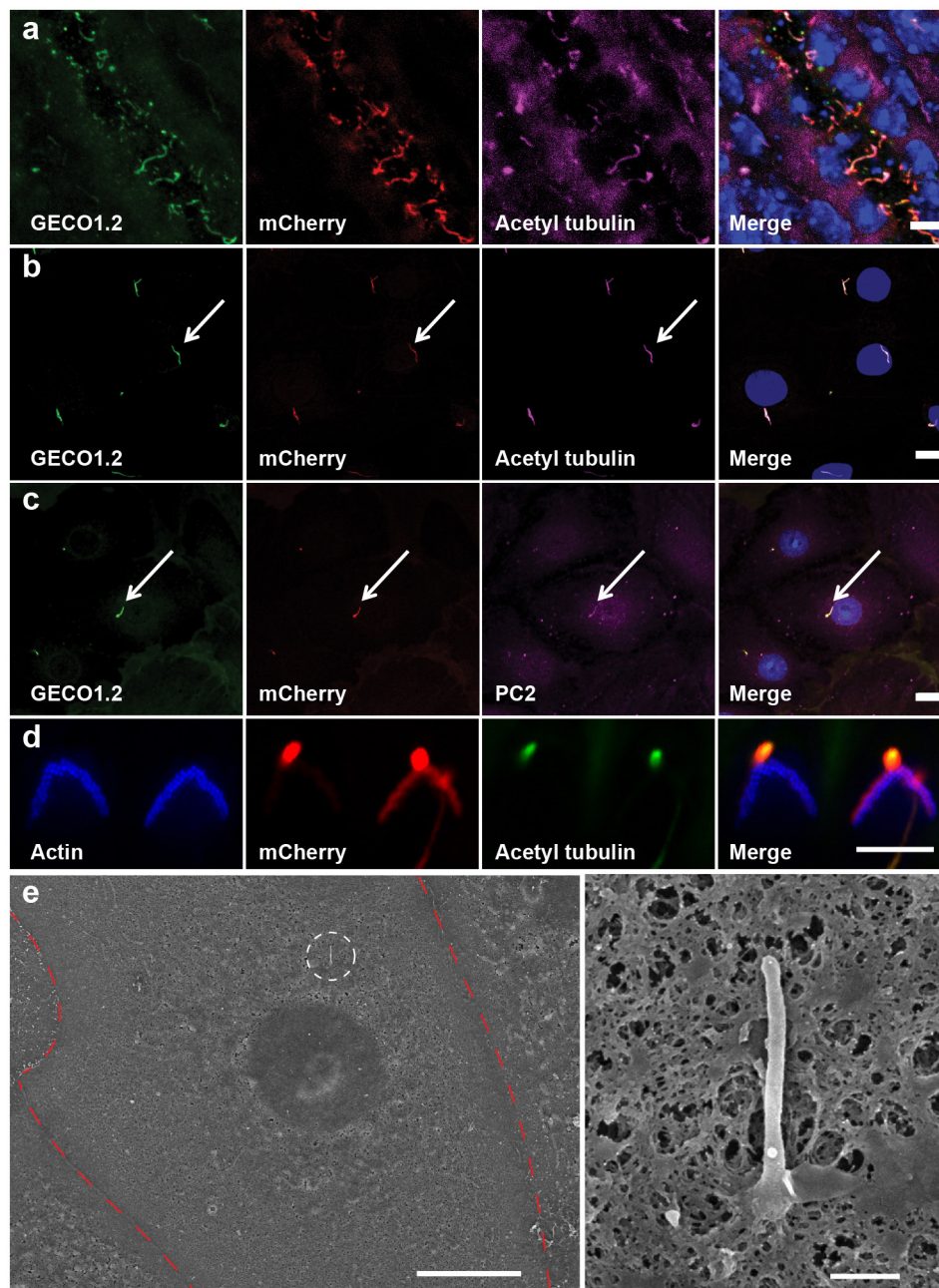
Channel alignment. Two factors contribute to misalignment of two channels during image acquisition: chromatic aberration from the optics and time delay due to sequential acquisition. For chromatic aberration, the two channels from each frame of a given time-lapse image were aligned using a translational transformation. A global translational transformation, derived from the individual frame transformations, was applied to all frames.

Object detection. Frame-by-frame superimposed images of both channels were created. When cilia motion was faster than acquisition time, channels were significantly misaligned. To create a combination image, two channels were added and smoothed using a Gaussian filter. Local image background was subtracted from the combination image, and Otsu thresholding used to detect objects. Small objects (less than three pixels) were filtered as noise.

Object tracking with ratio calculations. Different cilia in the same image vary with relative orientation. During flow application, many cilia undergo large deflections and even cross one another, further complicating the tracking of individual cilia. A tracking algorithm based on object overlap was implemented. It included features such as splitting of crossed cilia, linking cilia with no spatial overlap, and closing gaps over a given number of time frames. Once an individual cilium was tracked, the analysis code measured the signal of the cilium from both channels, calculated the ratio, and plotted it against time or spatial displacement.

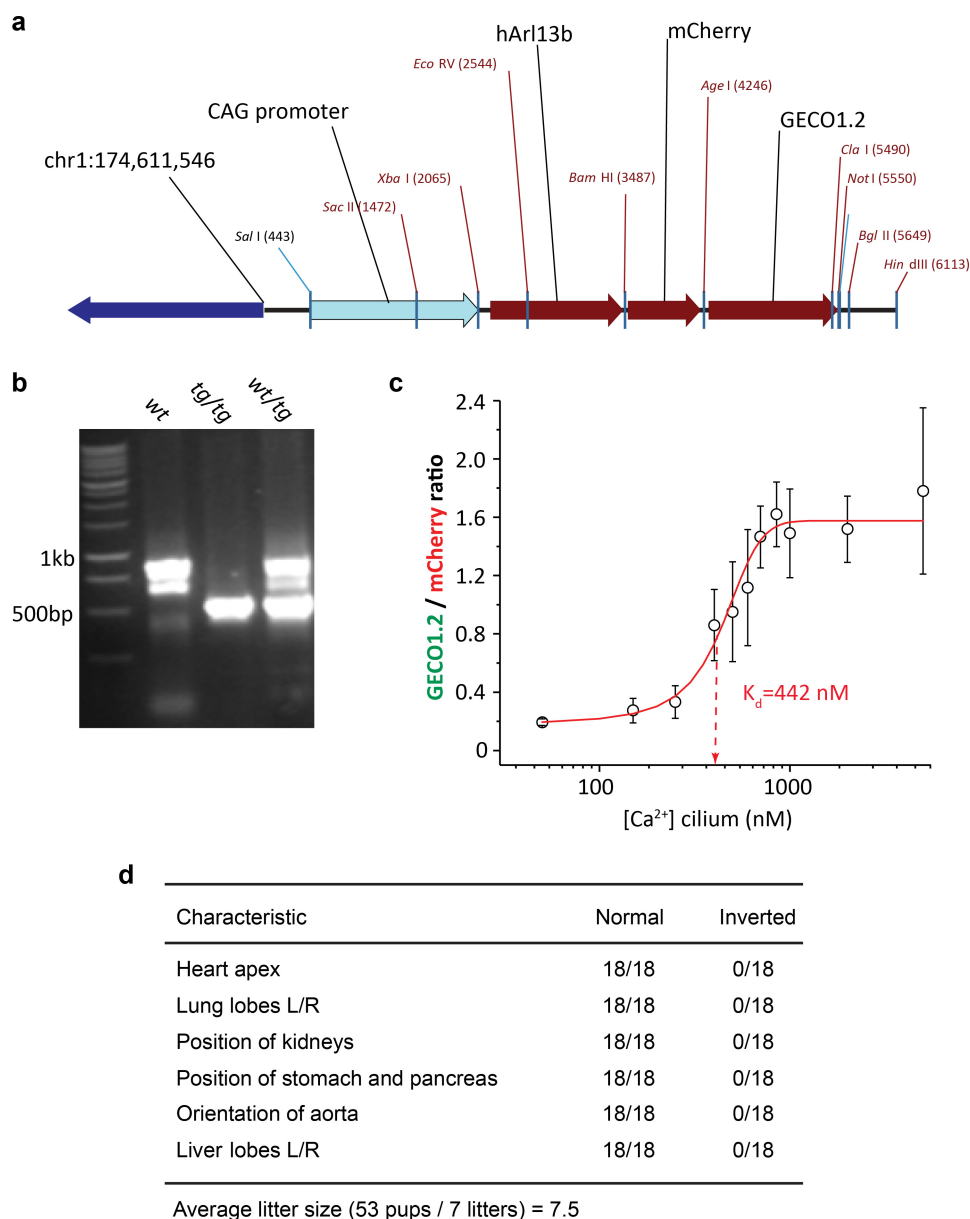
Code availability. The algorithms were developed in MATLAB in open-source, and are available upon request.

1. Faust, D. *et al.* Culturing primary rat inner medullary collecting duct cells. *J. Vis. Exp.* **76**, 50366 (2013).
2. Palmer, L. G. & Frindt, G. Gating of Na channels in the rat cortical collecting tubule: effects of voltage and membrane stretch. *J. Gen. Physiol.* **107**, 35–45 (1996).
3. Takao, D. *et al.* Asymmetric distribution of dynamic calcium signals in the node of mouse embryo during left-right axis formation. *Dev. Biol.* **376**, 23–30 (2013).
4. Downs, K. M. & Davies, T. Staging of gastrulating mouse embryos by morphological landmarks in the dissecting microscope. *Development* **118**, 1255–1266 (1993).
5. Yoshida, S. & Hamada, H. Roles of cilia, fluid flow, and Ca^{2+} signaling in breaking of left-right symmetry. *Trends Genet.* **30**, 10–17 (2014).
6. Zhao, Y. *et al.* An expanded palette of genetically encoded Ca^{2+} indicators. *Science* **333**, 1888–1891 (2011).
7. Spatz, J. M. *et al.* The Wnt inhibitor sclerostin is up-regulated by mechanical unloading in osteocytes in vitro. *J. Biol. Chem.* **290**, 16744–16758 (2015).
8. Xiao, Z. *et al.* Cilia-like structures and polycystin-1 in osteoblasts/osteocytes and associated abnormalities in skeletogenesis and Runx2 expression. *J. Biol. Chem.* **281**, 30884–30895 (2006).
9. Indzhukulian, A. A. *et al.* Molecular remodeling of tip links underlies mechanosensory regeneration in auditory hair cells. *PLoS Biol.* **11**, e1001583 (2013).
10. DeCaen, P. G., Dellinger, M., Vien, T. N. & Clapham, D. E. Direct recording and molecular identification of the calcium channel of primary cilia. *Nature* **504**, 315–318 (2013).
11. Nagasawa, H., Miyamoto, M. & Fujimoto, M. [Reproductivity in inbred strains of mice and project for their efficient production (author's translation)]. *Jikken Dobutsu* **22**, 119–126 (1973).
12. Yuan, S., Zhao, L., Brueckner, M. & Sun, Z. Intraciliary calcium oscillations initiate vertebrate left-right asymmetry. *Curr. Biol.* **25**, 556–567 (2015).
13. Tian, L. *et al.* Imaging neural activity in worms, flies and mice with improved GCaMP calcium indicators. *Nature Methods* **6**, 875–881 (2009).
14. Nagai, T., Yamada, S., Tominaga, T., Ichikawa, M. & Miyawaki, A. Expanded dynamic range of fluorescent indicators for Ca^{2+} by circularly permuted yellow fluorescent proteins. *Proc. Natl Acad. Sci. USA* **101**, 10554–10559 (2004).
15. Chen, T. W. *et al.* Ultrasensitive fluorescent proteins for imaging neuronal activity. *Nature* **499**, 295–300 (2013).



Extended Data Figure 1 | Arl13b-mCherry-GECO1.2 identifies primary cilia. Arl13b-mCherry-GECO1.2 contains an improved genetically encoded calcium indicator³⁶ (GECI) with an apparent K_d of 450 nM (Extended Data Fig. 2), well suited to work within the reported range of ciliary Ca^{2+} concentrations ($[\text{Ca}^{2+}]_{\text{cilium}}$)⁴⁰. The genomic integration site of the transgene is within a non-coding region of chromosome 1 (Extended Data Fig. 2) and transgenic animals maintained as homozygotes (*Arl13b-mCherry-GECO1.2*^{tg}) are viable, have average litter sizes, and do not show phenotypes consistent with cilia defects (for example, situs inversus, organ malformation; Extended Data Fig. 2). **a**, Frozen tissue section of P21 mouse kidney. GECO1.2 and mCherry are preferentially localized to cilia, identified by the cilia-specific marker,

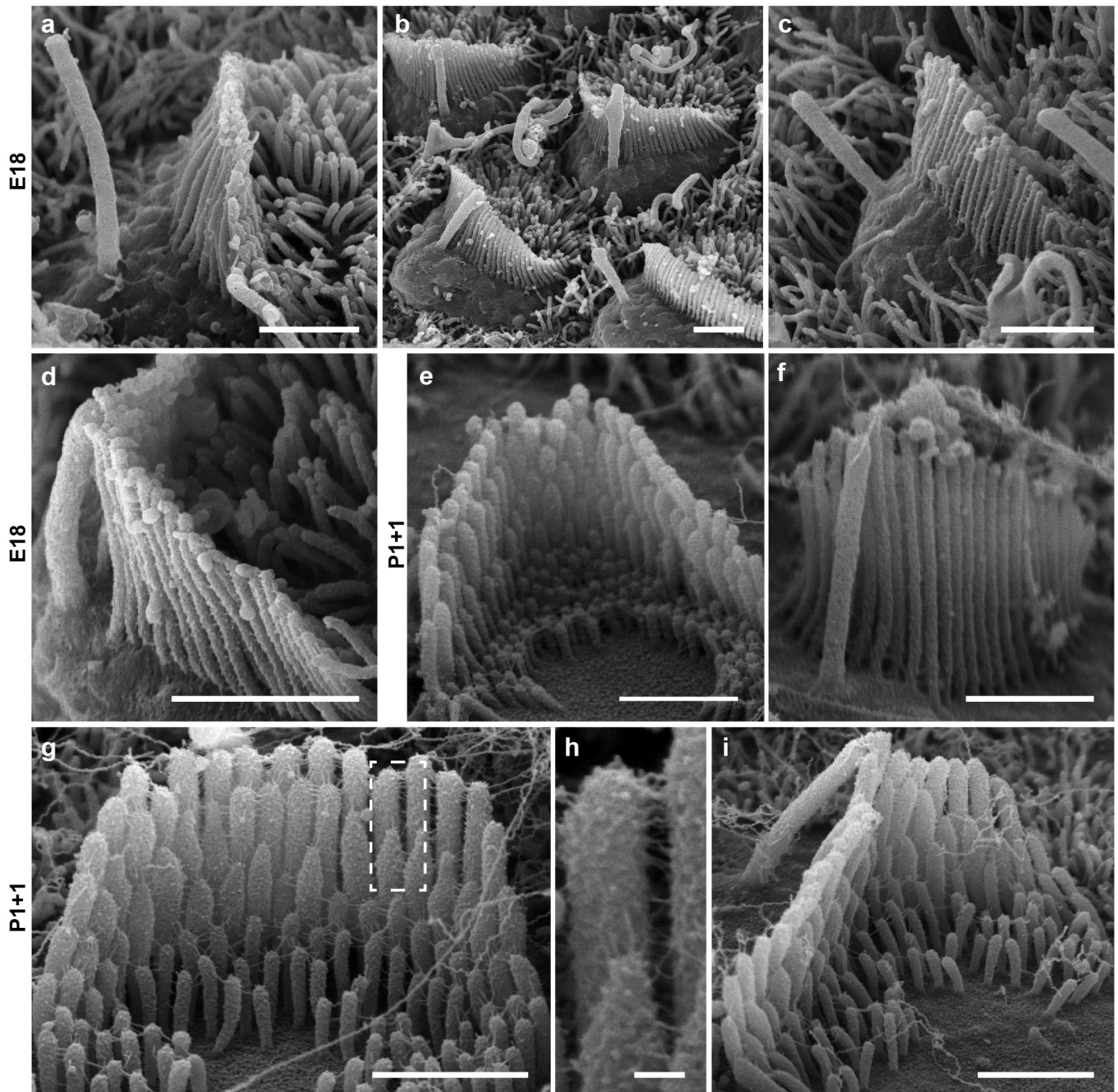
anti-acetylated tubulin antibody. **b**, **c**, Primary mIMCD cells isolated from kidneys of P14–P21 *Arl13b-mCherry-GECO1.2* transgenic mice. Ciliary localization (arrow) of anti-polycystin 2 antibody in **c**. Scale bars, 10 μ m. **d**, Two OHC hair bundles marked with the actin-binding peptide, phalloidin. One of the stereocilia bundles expresses Arl13b-mCherry-GECO1.2. Kinocilia on both OHCs marked with an antibody to acetylated tubulin, express Arl13b-mCherry-GECO1.2. Scale bar, 5 μ m. **e**, Scanning electron micrograph of a primary mIMCD cell. Left, red dashed line outlines a single mIMCD cell; white circle indicates the primary cilium. Scale bar, 10 μ m. Right, magnified image. No defects in cilia formation were evident following 3–4 days in culture. Scale bar, 500 nm. All images are representative of more than ten images taken of biological triplicates.



Extended Data Figure 2 | *Arl13b*-mCherry-GECO1.2 transgenic mouse.

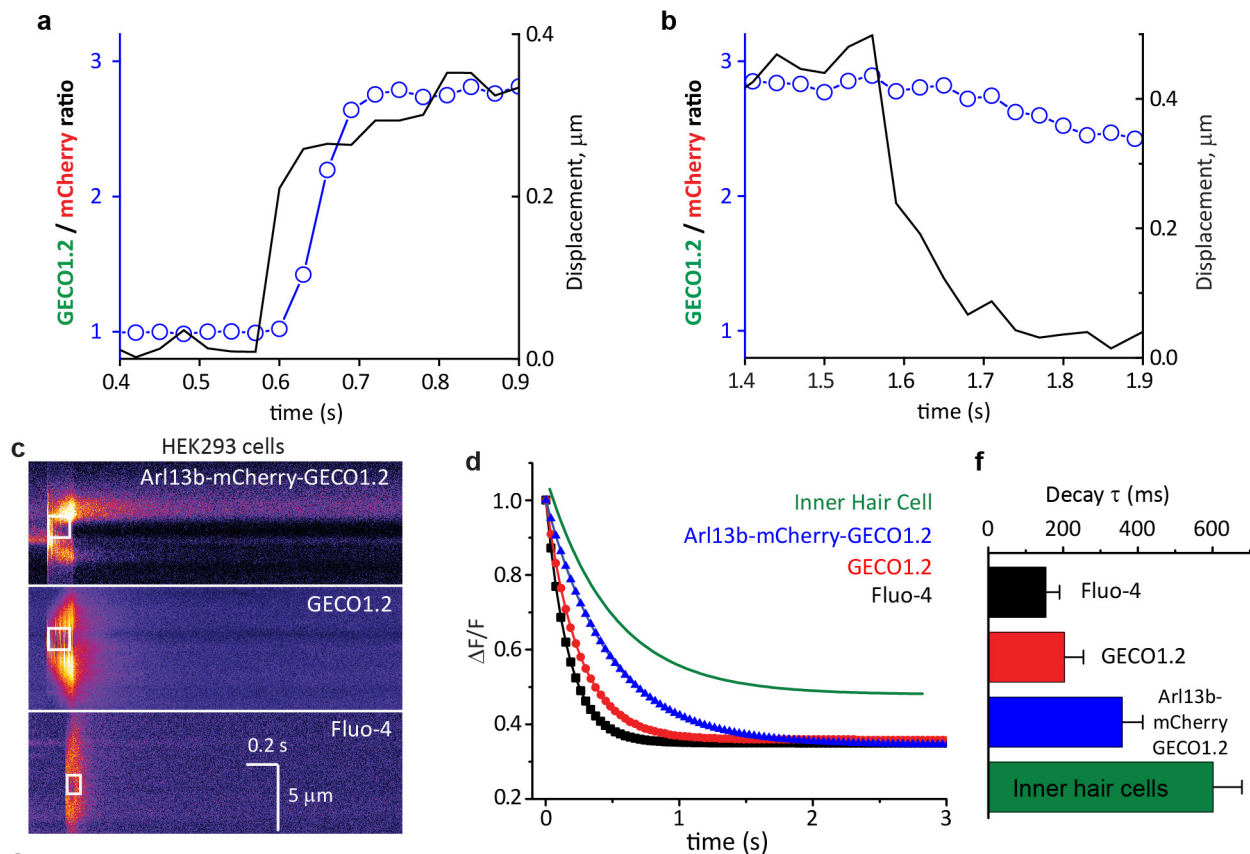
a, Transgene orientation and integration site. The transgene was integrated into the non-coding region of chromosome 1 (position 174,611,500).
b, The genotype of transgenic animals was determined by PCR using the following primers: 372-up, ACATGGCCTTTCTGCTCTC; 372-down, TTCAACATTTCCGTGTCGCC; and 944-down, GACATCTGTGGGAGGAGTGG. The PCR product for wild-type genomic sequence was ~600 bp; the transgene PCR product was ~400 bp.

c, mIMCD cells isolated from *Arl13b*-mCherry-GECO1.2^{tg} mice were imaged after permeabilization with 15 μ M digitonin in varying extracellular $[Ca^{2+}]$. Average ratios ($n = 12$ cilia per each data point) are plotted versus free $[Ca^{2+}]$. *Arl13b*-mCherry-GECO1.2 calibration fitted by a Boltzmann curve ($R^2 = 0.98$; $K_d = 442$ nM). **d**, Phenotype of *Arl13b*-mCherry-GECO1.2^{tg/tg} mice. Mouse organ morphology/orientation appeared normal (heterotaxy was not observed) and breeding animals had normal litter sizes (6–8 for C57Bl/6 (ref. 41)). All error bars \pm s.e.m.



Extended Data Figure 3 | *Arl13b-mCherry-GECO1.2^{tg/tg}* mouse organ of Corti hair cells develop normal stereocilia bundles. Hair bundles from *Arl13b-mCherry-GECO1.2^{tg/tg}* mice during development. **a–d**, Cochlear hair cells acutely dissected at age E18 appear normal. **a**, IHC, with kinocilium not attached to stereocilia. **b, c**, OHC stereocilia bundles with some kinocilia attached to the bundles. **d**, IHC bundle with kinocilium attached at tip. **e–i**, Cultured organ of Corti explant dissected

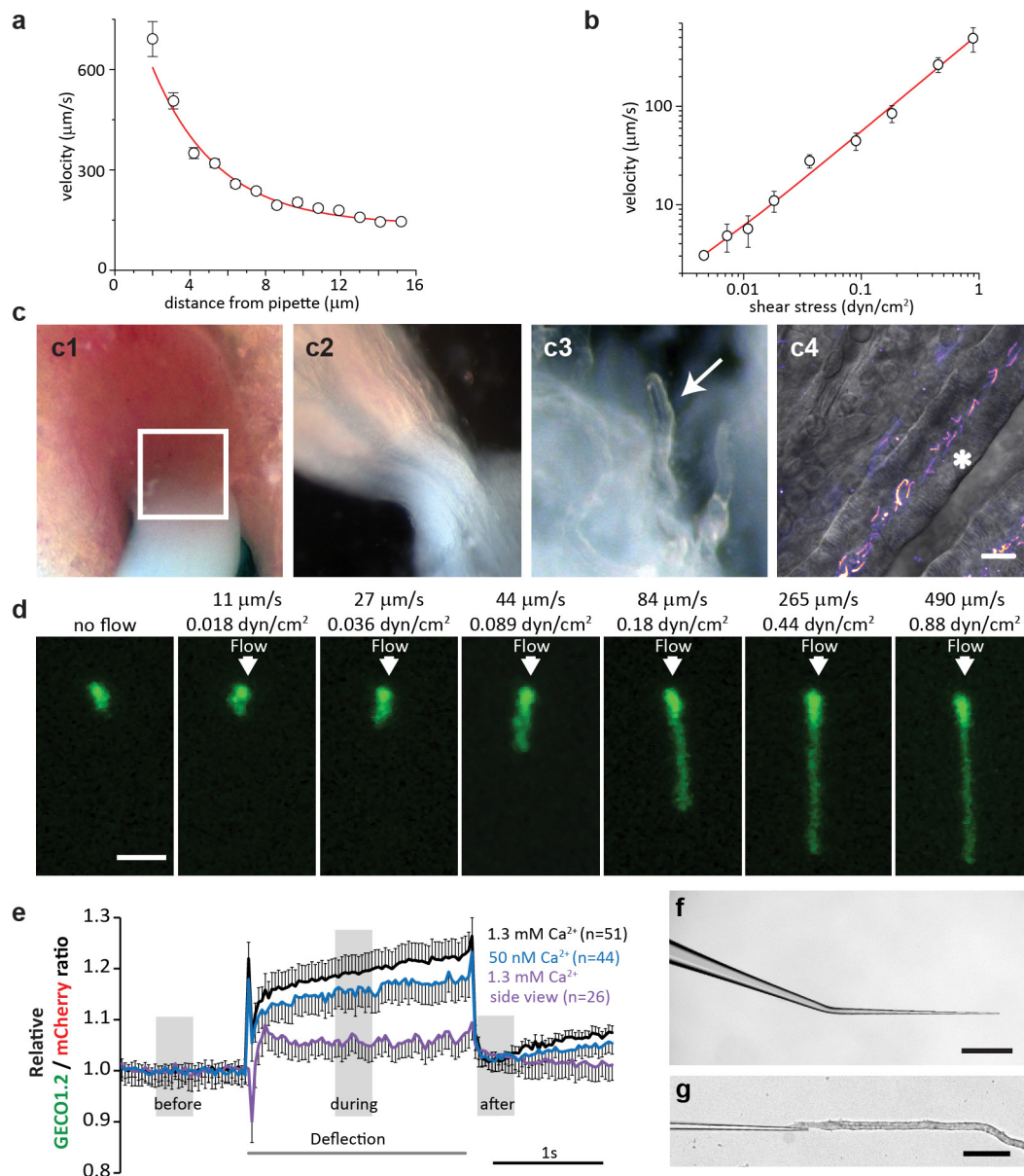
at P1 + 1 day *in vitro*. **e**, OHC with normal shape and stereocilia staircase structure. **f**, OHC stereocilia bundle with kinocilium. **g**, IHC with normal shape and stereocilia staircase structure; tip links and other links present. **h**, Pair of stereocilia (dashed box in **f**) at higher magnification. **i**, IHC with kinocilium attached at tip. Scale bars, 1 μm (except **h**, 100 nm). All images are representative of more than three images.



Indicator	Used by (reference)	τ rise (ms)	τ decay (ms)	k_D (bacterial protein)	k_D in vivo
GCAMP3	Jin et al., 2014, Delling et al., 2013	137 ± 4 (Chen et al., 2013)	597 ± 8 (Chen et al., 2013)	350 nM (Chen et al., 2013) 620 nM (Tian et al., 2009) 540 nM (Zhao et al., 2011)	~ 610 nM (Delling et al., 2013)
GECO1.2	Current manuscript	\sim GCaMP3 (Zhao et al., 2011)	600 (current study) 700 (Zhao et al., 2011)	1.2 μ M (Zhao et al., 2011)	440 nM (current study)
GCaMP5	Yuan et al., 2015	166 ± 20 (Chen et al., 2013)	667 ± 43 (Chen et al., 2013)	450 nM (Chen et al., 2013)	n.d.
GCaMP6 slow	Yuan et al., 2015	480 ± 24 (Chen et al., 2013)	1796 ± 73 (Chen et al., 2013)	150 nM (Chen et al., 2013)	n.d.
GCaMP6 fast	Current manuscript	80 ± 35 (Chen et al., 2013)	400 ± 41 (Chen et al., 2013)	375 nM (Chen et al., 2013)	n.d.
GECO1.1	Su et al., 2013	\sim GCaMP3 (Zhao et al., 2011)	680 (Zhao et al., 2011)	640 nM (Zhao et al., 2011)	n.d.
YC3.6 FRET	Lee et al., 2015	150 (Tian et al., 2009)	9000 (Tian et al., 2009)	250 nM (Nagai et al., 2004)	n.d.

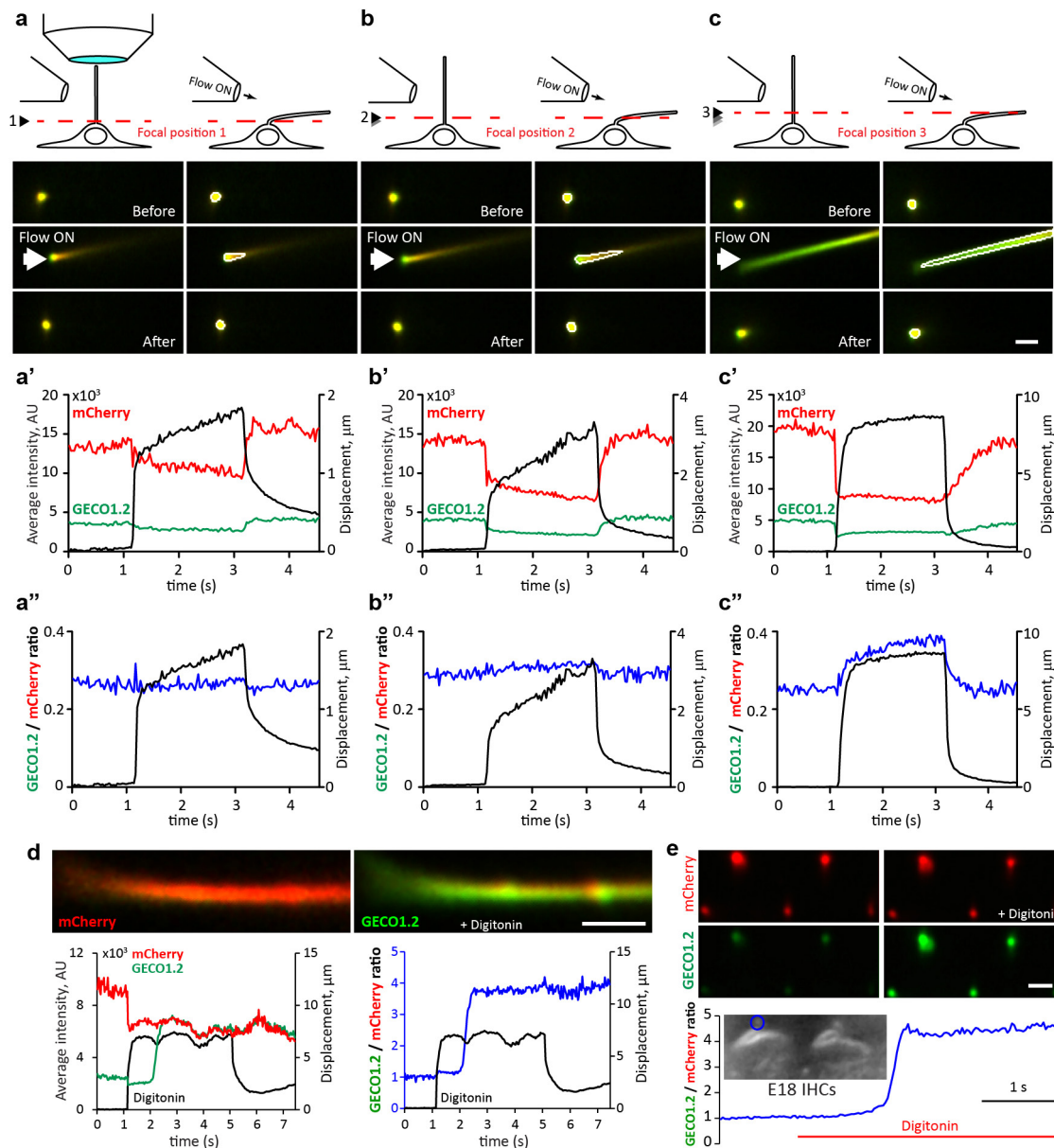
Extended Data Figure 4 | GECO1.2 k_{off} for Ca^{2+} dissociation from GECO1.2, measured in cells. **a**, **b**, Fig. 1g at higher time resolution. $F_{GECO1.2}/F_{mCherry}$ (open circles) relative to bundle motion (black line) at the initial deflection (**a**) and after return to the resting position (**b**). Bundle deflection preceded the $F_{GECO1.2}/F_{mCherry}$ increase by two frames (~ 60 ms). At the termination of the flow stimulus and return to the resting position, the ratio remained elevated owing to the slow decay ($\tau \approx 0.6$ s) of the Ca^{2+} from GECO1.2. **c**, Rapid Ca^{2+} uncaging was used to measure the Ca^{2+} decay rates for GECO1.2 (not bound to the membrane), Arl13b-mCherry-GECO1.2 (bound to the membrane), and the Fluo-4 control with its established time constant of decay. HEK293 cells were transfected with GECO1.2 or Arl13b-mCherry-GECO1.2 constructs and loaded with caged Ca^{2+} (NP-EGTA), or loaded with a combination of Fluo4-AM

and NP-EGTA. Caged Ca^{2+} was released by a local 100–200 ms pulse of ultraviolet laser illumination (white box); images were acquired in line scan mode (2 ms per vertical line). Representative of more than 16 images. **d**, Representative fitted fluorescence intensity decays of Fluo-4 in HEK293 cells (black), GECO1.2 (red), and Arl13b-mCherry-GECO1.2 (blue), compared with GECO1.2 from Arl13b-mCherry-GECO1.2 IHCs following deflection (green). **e**, Table summarizing molecular properties of genetically encoded calcium indicators (GECIs) used in current and previous reports describing ciliary Ca^{2+} signalling^{14–17,36,42–45}. **f**, Average decay rates, τ , for indicators in **c**, **d**. Fluo-4: $\tau = 154 \pm 36$ ms ($n = 16$); GECO1.2 in HEK293 cells: $\tau = 203 \pm 50$ ms ($n = 19$); Arl13b-mCherry-GECO1.2 in HEK293 cells: $\tau = 358 \pm 55$ ms ($n = 16$); Arl13b-mCherry-GECO1.2 in IHC stereocilia: $\tau = 601 \pm 70$ ms ($n = 10$). Averages \pm s.d.



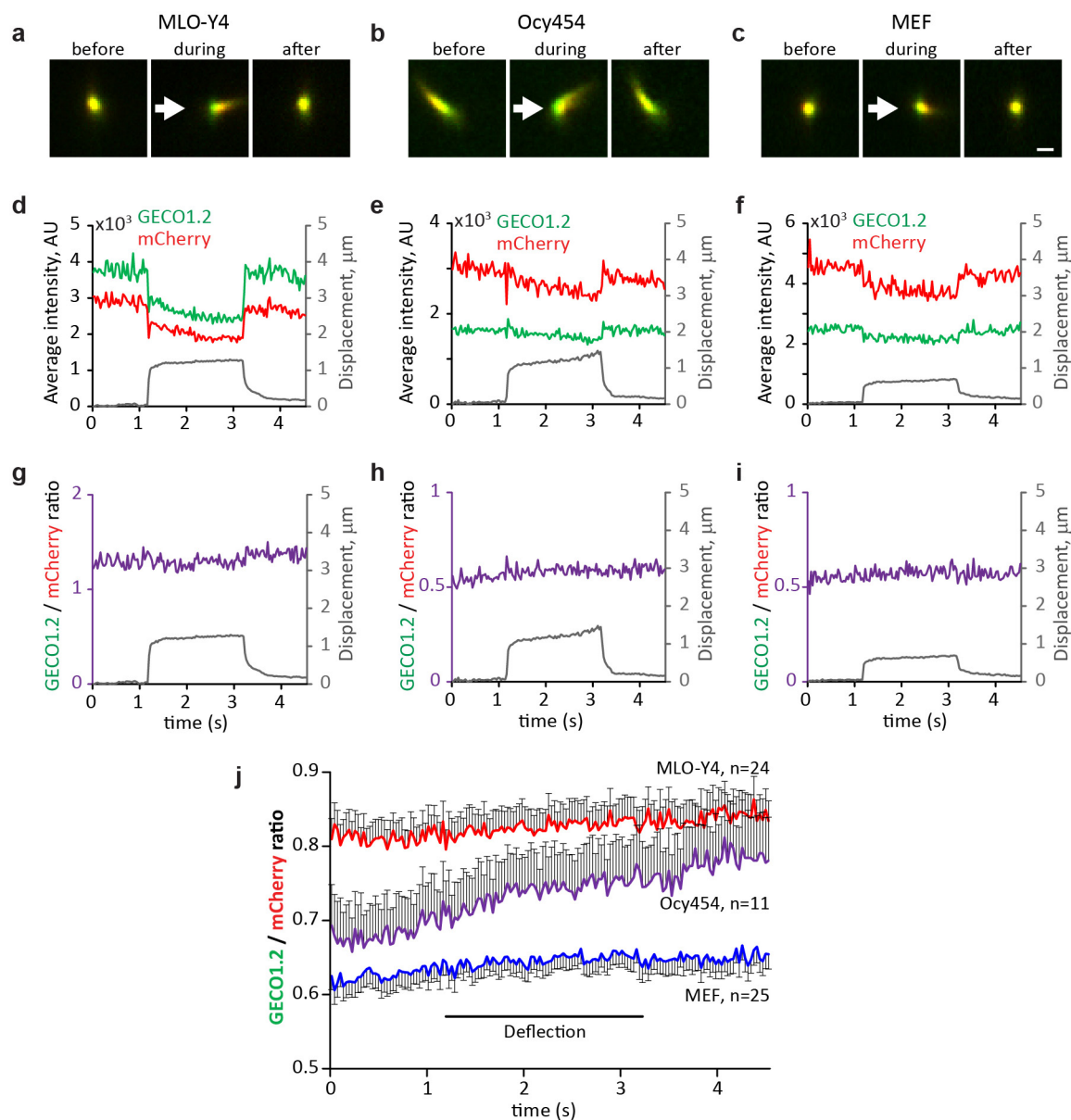
Extended Data Figure 5 | Kidney tubule dissection and flow velocity calibration. **a**, Calibration of the fluid velocity exiting the stimulus pipette versus distance from the mouth of the pipette (3- μm pipette, 6.4 mm Hg pressure step). The pipette was positioned $\sim 4\text{--}6\text{ }\mu\text{m}$ from the cilium, delivering a flow velocity of $250\text{--}300\text{ }\mu\text{m s}^{-1}$ ($n=5$). **b**, Velocity measured at the tip of the cilium and calculated shear stress at the plasma membrane ($n=6$). **c**, Microdissection of kidney tubules. **c1**, Coronal section of P15 kidney; white box indicates the microdissected area. **c2**, Area from **c1** following microdissection. **c3**, Small bundle of tubules; individual tubules gently separated from the bundle (arrow). **c4**, Tubules with thick walls and fluorescent cilia (asterisk) used for experiments. Scale bar, 5 μm . Images representative of more than six preparations. **d**, Maximum intensity z-projection of mIMCD primary cilia deflected in the flow chamber using defined fluid velocities. Scale bar, 3 μm ; representative of 14 cilia each with 7 z-stacks containing 12 frames. **e**, Relative ratio changes in primary mIMCD primary cilia during deflection, three experimental conditions. Black and blue lines represent the averaged normalized ratio changes for top views of cilia deflection in 1.3 mM and 50 nM $[\text{Ca}^{2+}]$, respectively.

The increase in ratio upon cilia deflection is comparable between high and low external $[\text{Ca}^{2+}]$, suggesting that the ratio change did not result from Ca^{2+} entry (Fig. 3h for P values). In addition, the return to baseline with cilium movement was much faster than the Ca^{2+} indicator response time, providing further evidence that it is a motion artefact. Such fast responses were not observed in the bona fide Ca^{2+} entry into IHC stereocilia (Fig. 2a and Extended Data Fig. 4b, d). Purple line represents the average normalized ratio changes for side-imaged cilia deflections in the presence of 1.3 mM $[\text{Ca}^{2+}]$. Ratio changes were negligible in side views, as the motion artefact (light path length change upon motion) is small. The positive slope seen in top views results from differential dye bleach, faster for mCherry than GECO1.2. Bleaching has a much more pronounced effect in top views, probably from the change in geometry, contribution from underlying autofluorescence, and relative light exposure upon bending. **f**, Micropipette used for cilia deflection inside the kidney tubules. Scale bar, 0.5 mm. **g**, Insertion of micropipette into the tubule. Scale bar, 100 μm . All error bars \pm s.e.m.



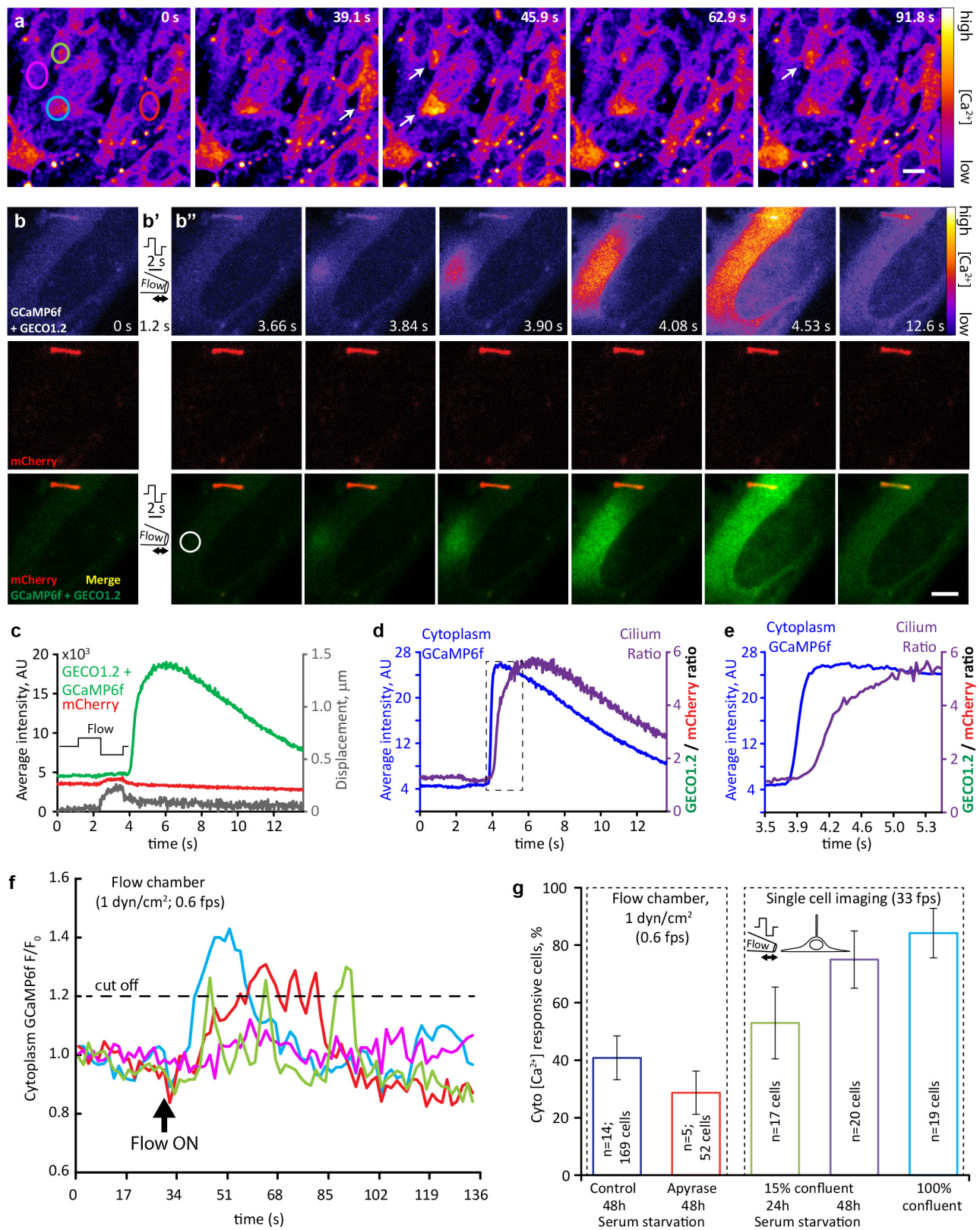
Extended Data Figure 6 | Deflection of primary cilia in the presence of 50 nM $[\text{Ca}^{2+}]$ reveals focal-plane-dependent artefact present in 'top view' imaging conditions; saturation controls for sensor. a–c, An mIMCD cell cilium was repeatedly deflected in a low (50 nM) $[\text{Ca}^{2+}]$ solution. The same flow stimulus (same pipette) was applied to the cilium while imaging in different focal planes. Top panels, experimental arrangement and fluorescence images of the cilium; red dashed lines indicate the focal plane for each set of images. Middle panels (a'–c'), average fluorescence intensity change for $F_{\text{GECO1.2}}$ (green) and F_{mCherry} (red) during deflection (black). Lower panels (a''–c''), ratio change (blue) during deflection (black). **a,** Primary cilium near its attachment to the cell. **b,** At a slightly higher focal plane, deflection enlarges the cross section of the cilium. **c,** A focal plane $\sim 1 \mu\text{m}$ above the cell surface. Different segments of the same cilium were imaged upon deflection. Note that the artefact increases with larger cross section changes. Thus, top view imaging of cilia is fraught with two interrelated artefacts: (1) at high

z -resolution ($0.8 \mu\text{m}$), the section of the cilia being imaged changes upon deflection, thus conflating fluorescence changes from different regions of the cilium; (2) at lower z -resolution, the path length, fluorescent indicator volume, and optical properties of the cilium above and below the image plane all change upon deflection and thus contribute to the apparent $[\text{Ca}^{2+}]$ reporter changes. **d, e,** Digitonin permeabilization indicates that the Arl13b–mCherry–GECO1.2 sensor is not saturated in measurements of primary cilia and kinocilia. Scale bars, $2 \mu\text{m}$. **d,** Top: mIMCD cell cilium deflected by fluid flow containing $10 \mu\text{M}$ digitonin. Bottom left: F_{mCherry} (red) decreased owing to cilia motion (black). $F_{\text{GECO1.2}}$ (green) rose ~ 1 s later, as permeabilization initiated Ca^{2+} influx. Right: $F_{\text{GECO1.2}}/F_{\text{mCherry}}$ increased ~ 4.2 -fold upon permeabilization. Representative of 13 videos \times 400 frames. **e,** Kinocilia of E15 cochlear hair cells. Digitonin ($10 \mu\text{M}$) increased the kinocilium's normalized $F_{\text{GECO1.2}}/F_{\text{mCherry}}$ ratio by 4.6-fold. Representative of 6 videos \times 400 frames. Similar results were obtained in P3 hair cell kinocilia (data not shown).



Extended Data Figure 7 | No change in $[Ca^{2+}]_{\text{cilium}}$ during mechanical stimulation of primary cilia in MLO-Y4 and Ocy454 osteocyte-like cells, and primary MEF cells. a–c, Cultured MLO-Y4 (a, representative of 24 videos \times 150 frames), Ocy454 (b, representative of 11 videos \times 150 frames), and MEF cells isolated from E14 *Arl13b-mCherry-GECO1.2^{tg}; GCaMP6f^{tg}; E2a-Cre^{tg}* mice (c, representative of 25 videos \times 150 frames) were imaged from above; stimulus pipette was placed ~ 4 – 6 μm away from the cilium. Images: cilium before, during, and after deflection by a 2 s, $\sim 250 \mu\text{m s}^{-1}$ flow stimulus. The ROI was identified frame-by-frame by a MATLAB tracking algorithm and $F_{\text{GECO1.2}}$ and F_{mCherry} quantified. Scale bar, 1 μm . d–f, Quantification of the channel intensities from the

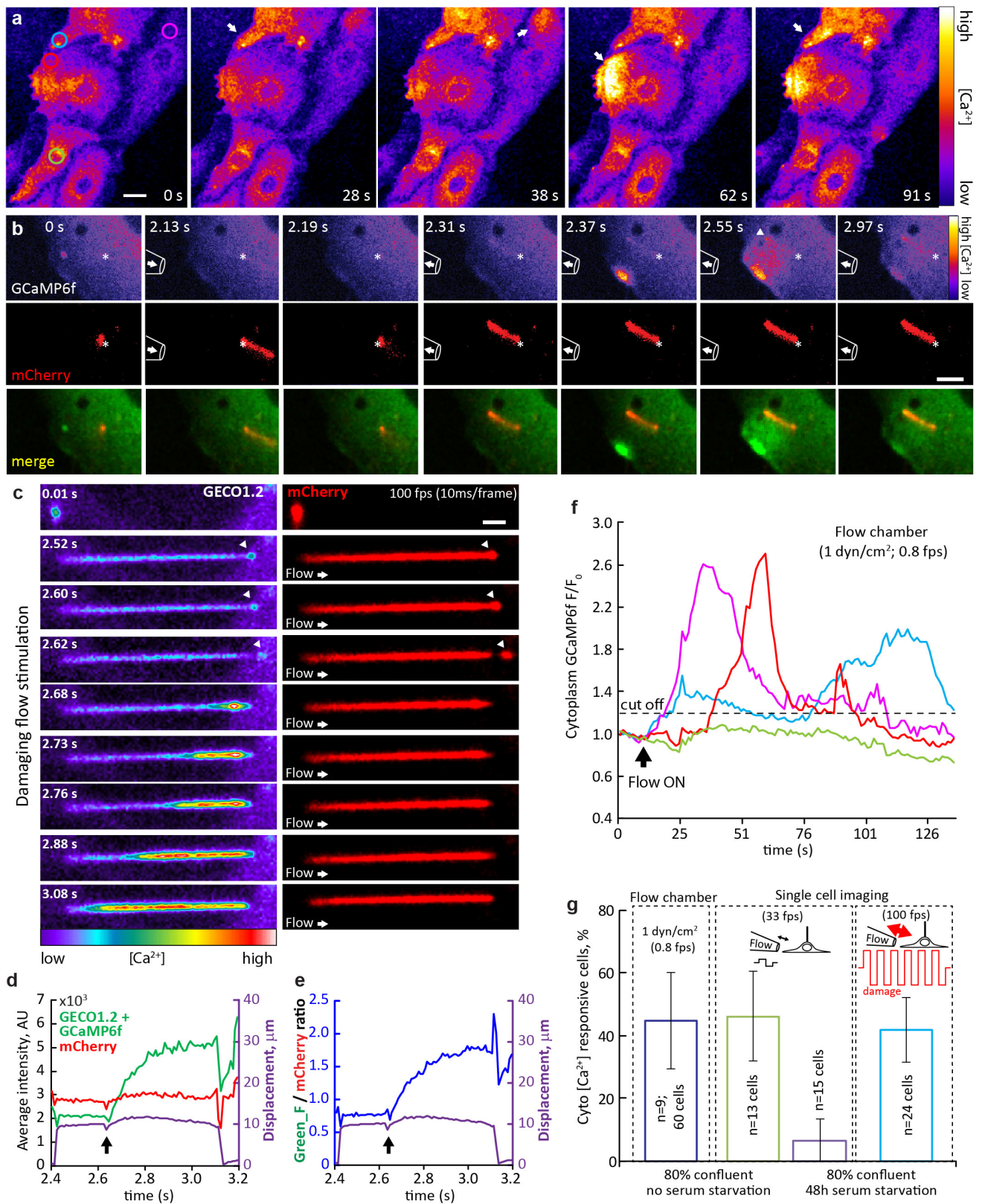
cilia in a–c. Average fluorescence intensity for both $F_{\text{GECO1.2}}$ and F_{mCherry} decreased as the cilia flattened and the light path length via the cilium volume changed. Cilium ROI displacement is superimposed in grey. g–i, Ratioing $F_{\text{GECO1.2}}$ and F_{mCherry} compensated for the path-length artefact (see also Extended Data Fig. 6), revealing no change in $[Ca^{2+}]$ during deflection. Cilium ROI displacement is superimposed in grey. j, Average $F_{\text{GECO1.2}}/F_{\text{mCherry}}$ for MLO-Y4 (red, $n = 24$), Ocy454 (purple, $n = 11$) and MEF (blue, $n = 25$) primary cilia. The small continuous positive slope during the entire course of the experiment results from differential dye bleaching ($\text{mCherry} > \text{GECO1.2}$). All error bars \pm s.e.m.



Extended Data Figure 8 | See next page for caption.

Extended Data Figure 8 | Flow-dependent $[Ca^{2+}]$ increases originate in the cytoplasm in MEF cells. **a**, Representative image sequence of cultured MEF cells responding to 1 dyn cm^{-2} fluid flow in a flow chamber. Cells were isolated from E14 *Arl13b-mCherry-GECO1.2^{tg};GCaMP6f^{tg};E2a-Cre^{tg}* mice, expressing *Arl13b-mCherry-GECO1.2* in primary cilia, and GCaMP6f in the cytoplasm. $F_{GCaMP6f}$ is presented as pseudocolour heatmap; arrows point to the cells that respond to the flow stimulus, circles indicate ROI used for analysis in **f**; imaging rate, 0.6 f.p.s.; scale bar, $10 \mu\text{m}$. Representative of 19 videos \times 60 frames. **b–b''**, Representative image sequence of cultured MEF cell responding to a single cycle of oscillatory fluid flow (OscFF¹⁶). Top row, $F_{GCaMP6f} + F_{GECO1.2}$ presented as pseudocolour heatmap. Middle row, mCherry fluorescence. Bottom row, merged $F_{GCaMP6f} + F_{GECO1.2}$ (green) and $F_{mCherry}$ (red) signals. Left panel, **b**, average of about ten consecutive frames before stimulus application; 1.2 s into the experiment, an alternating pressure stimulus was applied to the cell membrane, away from the cilium (positive, then negative, ~ 1.5 s each, diagram shown in **b'**). Following the stimulus (**b''**; each image is an average of three to five consecutive frames at the time point reflected on the image), a Ca^{2+} wave originating from the plasma membrane/cytoplasm spreads across the cell body. As seen on the image sequence, a single cycle of strong OscFF application to the cell membrane initiates a Ca^{2+} increase in the cytoplasm (whether from across the plasma membrane or from intracellular stores was not determined). Negligible cilium movement has been detected in this particular case ($\sim 200 \text{ nm}$, grey trace in **c**), as the cilium was located under the cell, between the cell and the coverslip. Scale bar, $5 \mu\text{m}$. Representative of 40 videos \times 450 frames.

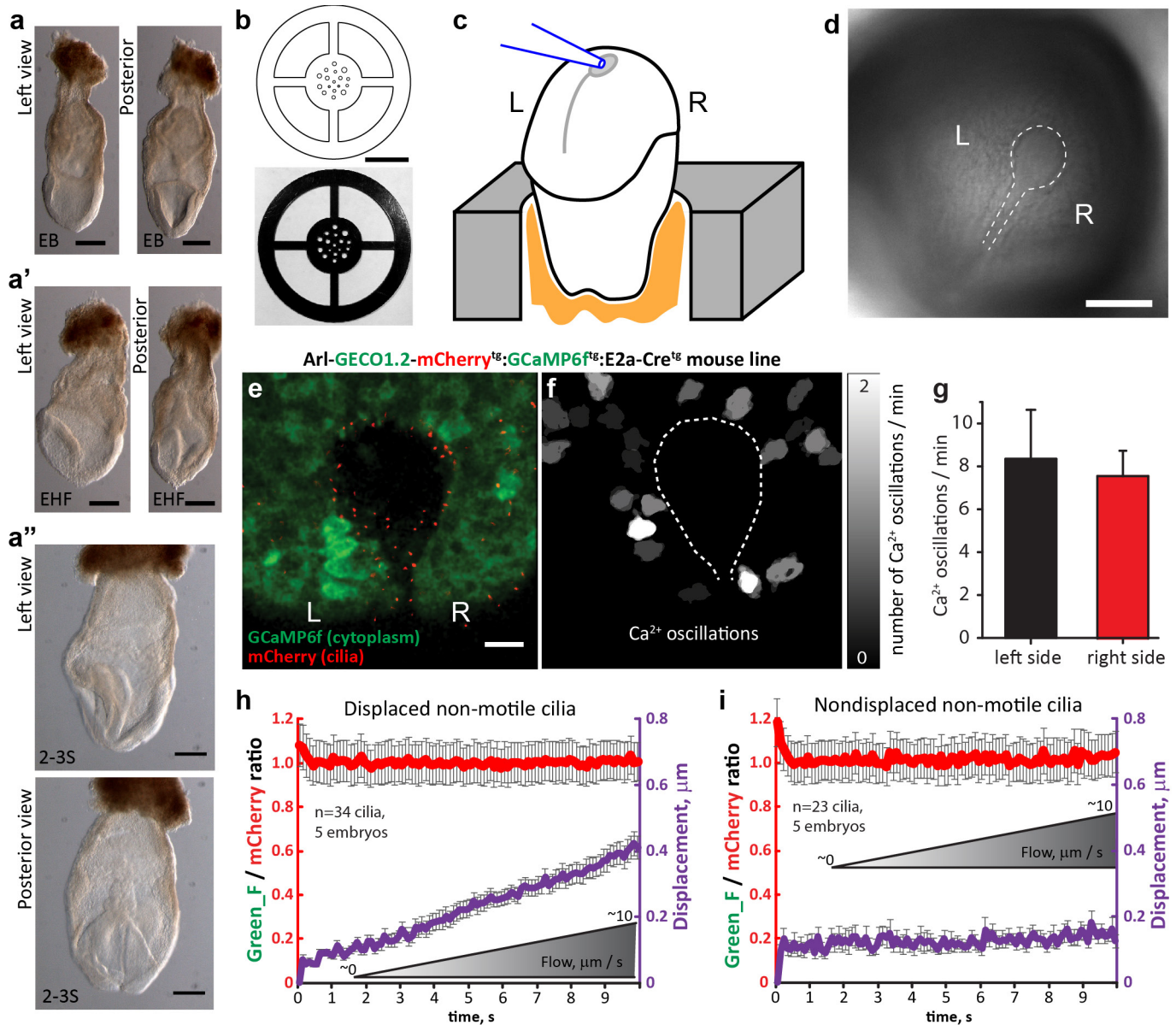
c, Quantification of ($F_{GECO1.2} + F_{GCaMP6f}$) (green) and $F_{mCherry}$ (red) channel intensities in the cilium in **b**. The ROI was identified frame-by-frame by a MATLAB tracking algorithm and average fluorescence plotted as a function of time. Cilium ROI displacement is superimposed in grey. **d**, Average $F_{GCaMP6f}$ (cytoplasm) in the ROI depicted in **b'** (white circle), superimposed with ciliary ($F_{GECO1.2} + F_{GCaMP6f}$) / $F_{mCherry}$ (purple trace) showing an earlier Ca^{2+} onset for the cytoplasmic GCaMP6f indicator. Dashed box outlines the data shown in **e**. **e**, Same as in **c**, but with higher time resolution. Ciliary $[Ca^{2+}]$ increase is $\sim 200 \text{ ms}$ delayed from the cytoplasmic Ca^{2+} increase, showing the necessity for high imaging rates for Ca^{2+} imaging of cilia. **f**, Quantification of $F_{GCaMP6f}$ change over time for four cells from **a**; ROIs depicted in **a**. Dashed line: threshold for labelling a cell as responsive (20% change in fluorescent intensity). All selected cells, except that represented by the magenta trace, responded to the flow. **g**, MEF cell response rate in flow chamber and pipette flow application experiments. Blue and red bars represent 1 dyn cm^{-2} application in flow chamber experiments; $\sim 40\%$ of the cells responded to the flow. Apyrase (7 units per millilitre) application did not change the response rate, suggesting that ATP release is not a major contributor to flow-induced Ca^{2+} response in this cell type. Remaining bars represent single-cell imaging experiments with local flow delivery via pipette, using cells in three conditions: low confluency cells ($\sim 15\%$), with 24 h (green bar) and 48 h (purple bar) serum starvation to promote cilia formation, and highly confluent coverslips without serum starvation (light blue bar). Arrest of MEF cells in G0 sensitizes cells to respond to flow stimulus with intracytoplasmic Ca^{2+} changes. All error bars \pm s.e.m.



Extended Data Figure 9 | See next page for caption.

Extended Data Figure 9 | Flow-dependent $[Ca^{2+}]$ increases originate in the cytoplasm in primary mIMCD cells. **a**, Cultured primary mIMCD cells, isolated from *Arl13b-mCherry-GECO1.2^{tg}:GCaMP6f^{tg};E2a-Cre^{tg}* mice, respond to 1 dyn cm^{-2} shear stress in a flow chamber. F_{GCaMP6f} fluorescence intensity is presented as pseudocolour heatmap. Arrows point to the cells that respond to the flow stimulus. Imaging rate, 0.8 f.p.s.; scale bar, $10 \mu\text{m}$. Representative of 6 videos \times 100 frames. Circles indicate ROIs used for analysis in **f**. **b**, Cultured mIMCD cell with cytoplasmic Ca^{2+} oscillations following flow application. Pipette outline on the image represents its approximate position; an arrow inside the pipette represents the direction of the flow. An alternating flow stimulus deflects the primary cilium (red) in positive and negative directions. This deflects the cell membrane, resulting in Ca^{2+} increases in the cytoplasm. Although it is well known that mechanical force can initiate increases in cytoplasmic Ca^{2+} , there are several potential sources (plasma membrane rupture, mechanosensitive ion channels, ATP release and purinergic receptor activation, intracellular Ca^{2+} stores) that appear to depend on cell type and conditions. No change in ciliary $[Ca^{2+}]$ is evident until the cytoplasmic Ca^{2+} reaches the cilium (arrowhead, 2.55 s). Top row, $F_{\text{GCaMP6f}} + F_{\text{GECO1.2}}$ presented as a pseudocolour heatmap. Middle row, mCherry signal intensity. Bottom row, merged $F_{\text{GCaMP6f}} + F_{\text{GECO1.2}}$ (green) and F_{mCherry} (red). Asterisks indicate the base of the cilium. Imaging rate, 33 f.p.s.; scale bar, $5 \mu\text{m}$. Representative of 17 videos \times 450 frames. **c**, Fast imaging during supraphysiological flow application to primary cilium of cultured mIMCD

cells reveals ciliary damage and subsequent increase of ciliary $[Ca^{2+}]$. $F_{\text{GCaMP6f}} + F_{\text{GECO1.2}}$, pseudocolour heatmap (left); F_{mCherry} , red (right). At flow rates greater than ten times those used for ciliary deflection, the ciliary membrane disintegrates and distal parts of the cilium (arrowheads) detach. Following ciliary tip damage, Ca^{2+} enters the cilium from the break point. Ciliary Ca^{2+} influx does not occur before detachment of ciliary tip, presumably when the membrane experiences the highest force and stretch. Arrow, direction of the flow. Imaging rate, 100 f.p.s.; Scale bar, $2 \mu\text{m}$. Representative of 13 videos \times 3,000 frames. **d**, **e**, Quantification of $F_{\text{GCaMP6f}} + F_{\text{GECO1.2}}$ and F_{mCherry} from the cilium in **c**. Arrow, ciliary tip detachment event. The ROI was identified frame-by-frame by a MATLAB tracking algorithm and $F_{\text{GECO1.2}}$ and F_{mCherry} (**d**) and ratio (**e**) plotted as a function of time. Cilium ROI displacement is superimposed (purple). **f**, Quantification of $F_{\text{GECO1.2}}$ and F_{mCherry} fluorescence intensity change over time for four representative cells in **a**; ROIs depicted in **a** (left). Dashed line, 20% threshold defining responsive cells. All selected cells (except that represented by the green trace) responded to flow. **g**, Cultured primary mIMCD cell response rate in flow chamber and pipette flow application experiments. Blue bar, flow application performed in a flow chamber; $\sim 46\%$ of the cells respond to 1 dyn cm^{-2} shear stress. Green and purple bars represent single-cell imaging experiments for highly confluent cells ($\sim 80\%$), without (green bar) or following (purple bar) 48 h serum starvation. Light blue bar, cells following 48 h serum starvation in response to damaging flow stimulus. All error bars \pm s.e.m.



Extended Data Figure 10 | Cytoplasmic Ca^{2+} signalling in the embryonic node of *Arl13b-mCherry-GECO1.2^{tg}; GCaMP6f^{tg}; E2a-Cre^{tg}* embryos. **a–a''**, Representative images of embryos within the developmental window used: from early bud (EB, **a**), early headfold (EHF, **a'**) to two- to three-somite stage (2–3S, **a''**). Scale bars, 200 μm . Each panel is a representative of at least five images. **b**, Drawing (top modified after ref. 22) and image (bottom) of the embryo mounting plate used for imaging. Scale bar, 10 mm. **c**, Embryos were mounted with the node facing up. Pipette used for cilia deflection is shown in blue. **d**, Differential interference contrast image of embryo with the node outlined by the dashed line. Scale bar, 100 μm . Representative of 14 images. **e**, Representative image of an embryonic node of an *Arl13b-mCherry-GECO1.2^{tg}; GCaMP6f^{tg}; E2a-Cre^{tg}* EHF embryo, expressing GCaMP6f in the cytoplasm to visualize cytoplasmic Ca^{2+} oscillations. Scale bar, 20 μm . Representative of 3 videos \times 300 frames. **f**, Mapping of cytoplasmic Ca^{2+} oscillations in close proximity to the embryonic node. Only $\Delta F/F > 30\%$

were included in the analysis. Nodal perimeter is outlined with white dashed line. **g**, Quantification of cytoplasmic Ca^{2+} signals shown in **e**, **f** occurring within 0.01 mm² on either the left or the right side of the embryonic node. Left side: $8.3 \pm 2.3 \text{ min}^{-1}$; right side: $7.6 \pm 1.2 \text{ min}^{-1}$; $n = 5$ embryos; this difference was not statistically significant between the late bud and late headfold (LHF) stage (see also ref. 33) (Supplementary Video 10). **h**, **i**, Average ratio changes ($F_{\text{GECO1.2}}/F_{\text{mCherry}}$) of crown cell primary cilia from the left side of the embryonic node of *Arl13b-mCherry-GECO1.2^{tg}; GCaMP6f^{tg}; E2a-Cre^{tg}* expressing EHF embryos during the application of physiological levels of flow (slow deflection; note longer imaging time of 15 s). Flow velocity, calibrated in-frame using fluorescent beads, was slowly increased (ramped); see also Fig. 4 k, l. Cilia were divided into two groups: **h**, the average ratio change for displaced cilia ($n = 34$ cilia from 5 embryos; average centroid displacement was $409 \pm 35 \text{ nm}$); **i**, the average ratio change for non-displaced cilia ($n = 23$ cilia from 5 embryos). All error bars \pm s.e.m.